COMPUTATION OF SUPERSONIC AND LOW SUBSONIC CASCADE FLOWS USING AN EXPLICIT NAVIER-STOKES TECHNIQUE AND THE k-ε TURBULENCE MODEL

R. F. Kunz, B. Lakshminarayana
Department of Aerospace Engineering
Pennsylvania State University
University Park, PA, 16802

ABSTRACT

A fully explicit two-dimensional flow solver, based on a four-stage Runge-Kutta scheme, has been developed and utilized to predict two-dimensional viscous flow through turbomachinery cascades for which experimental data is available. The formulation is applied to the density averaged Navier-Stokes equations. Several features of the technique improve the ability of the code to predict high Reynolds number flows on highly stretched grids. These include a low Reynolds number compressible form of the k-ε turbulence model, anisotropic scaling of artificial dissipation terms and locally varying timestep evaluation based on hyperbolic and parabolic stability considerations. Comparisons between computation and experiment are presented for both a supersonic and a low-subsonic compressor cascade. These results indicate that the code is capable of predicting steady two-dimensional viscous cascade flows over a wide range of Mach numbers in reasonable computation times.

NOMENCLATURE

Symbols Used

a	speed of sound
c	chord length
c_p	specific heat at constant pressure
C_f	skin friction coefficient
C_p	pressure coefficient
e	internal energy per unit mass

e_o	total energy per unit mass (= e + $V^2/2$)
E, F	flux vectors
U,V	contravariant velocity components
J	Jacobian of curvilinear transformation
k	turbulent kinetic energy
L	turbulence length scale
n, s	blade normal and tangential coordinates
p	static pressure
Pr	Prandtl number
q_i	cartesian components of heat transfer rate vector
Q	primary transport variable vector
R	residual vector
S	source term vector
t	pitch length
T	static temperature
T_u	turbulence intensity
u, v	cartesian velocity components
V	magnitude of total velocity
x, y	cartesian coordinates
α	exponent in artificial dissipation scaling function
β_1, β_2	incidence and deviation angles
δ_{ij}	Kronecker delta
$\delta_{\xi\xi}$, $\delta_{\eta\eta}$, $\delta_{\xi\xi\xi\xi}$, $\delta_{\eta\eta\eta\eta}$	central differencing operators
δ_1, δ_2	displacement and momentum thickness
γ	specific heat ratio
Δt	local timestep
ε	isotropic turbulent kinetic energy dissipation rate
κ_2, κ_4	artificial dissipation constants
μ_l, μ_t	molecular and turbulent viscosities
ν_{ij}	pressure monitoring parameter for artificial dissipation
ξ, η	curvilinear coordinates
ρ	density
σ_2, σ_4	artificial dissipation weighting functions
τ_{ij}	cartesian components of stress tensor
ω	total pressure loss coefficient

Superscripts and Subscripts Used

c	convective
i, j	grid indices in streamwise and pitchwise directions respectively
l	laminar
m	cascade mean value (average of inlet and outlet quantities)
o	stagnation
t	turbulent
v	viscous
w	wall
θ	cascade pitchwise direction
∞	inlet freestream
$\hat{}$	quantity scaled by metric Jacobian
'	fluctuating quantity in time averaging
"	fluctuating quantity in density averaging
~	density averaged quantity
-	time averaged quantity

INTRODUCTION

Computation of viscous flows by numerically solving the Navier-Stokes equations has become increasingly feasible due in most part to the ever increasing speed and memory of digital computers. State of the art CFD codes available today are capable of calculating steady 3-D viscous flows about entire vehicles, and even unsteady viscous flows in 3-D turbomachinery stages. However, despite the rapid advance towards exploiting the power of computers now available, some serious limitations of these codes have yet to be adequately resolved. Surely the most profound of these limitations is the lack of accurate, general turbulence models. Secondary to this, but of much concern, is the role of artificial dissipation in Navier-Stokes calculations.

Explicit schemes, such as the Runge-Kutta methods first applied to the solution of the Euler equations by Jameson, Schmidt and Turkel[1] offer several appealing characteristics in application to fluid flow computations. Such schemes are easily vectorizable, amenable to convergence acceleration techniques,

and can be extended to unsteady flow computations in a straightforward manner. However, because of the stiffness associated with the explicit treatment of transport equations which contain large source terms, incorporation of higher order turbulence models, which contain such source terms, has not been popular in explicit flow solvers.

Often, algebraic eddy viscosity models are used to approximate the apparent stresses in explicit codes. These models have little computational overhead and do not adversely affect the stability of the scheme. Though very useful in computing attached or slightly separated boundary layer flows, such models have well recognized drawbacks in the computation of complex flows where multiple length scales exist and where the transport of turbulent length scales is important. Though the k-ε turbulence model also has major deficiencies [see Speziale[2], Lakshminarayana[3] for example], it does provide the transport of length scale which is computed based on local fluid and turbulence properties. The model has been shown to provide better predictions than algebraic models for 2-D flow with adverse pressure gradient [Kirtley and Lakshminarayana[4]] and for 2-D shock-boundary layer flow on curved surfaces [Degrez and VanDromme[5]]. It therefore seemed worthwhile to try to use it to provide an improved engineering approximation to the complex cascade flowfields investigated herein.

Implicit flow solvers have been used for well over a decade to compute compressible turbulent flows using various forms of the k-ε turbulence model. However, there have been only a few attempts to incorporate the model into an explicit solution procedure. In these cases, the stiffness problems associated with explicit treatment of the k-ε model have been circumvented by incorporating semi-implicit treatment of the source terms [Liu[6]], implementation of an algebraic inner layer model coupled to a high Reynolds number form of the k-ε model in the outer layer [Liu[6]], or by using wall functions to model, rather than to resolve, the near wall region where source terms and grid aspect ratio can be large [Grasso and Speziale[7], Eliasson[8], Holmes and Connell[9]].

The use of higher order turbulence models, and the precise control of levels of artificial dissipation, can improve the accuracy of high Reynolds number flow computations about complex configurations. The main thrust of this investigation is the incorporation of a low Reynolds number compressible form of the k-ε turbulence model into a purely explicit scheme, and the application of the technique to flows across a wide range of Mach numbers. In addition to this, some recently published improvements in controlling artificial dissipation levels in the computation of viscous flows on highly stretched grids are tested and incorporated. Two complex cascade flows are computed, for supersonic and low subsonic freestream conditions. For the supersonic cascade, isentropic blade Mach number, shock-boundary layer structure and wake loss profiles are compared with experimentally measured values. Pressure distribution and boundary layer profiles of velocity and turbulent kinetic energy are compared with data for the subsonic

cascade. The results are shown to be quite good within the accuracy of the turbulence model and experimental data used.

GOVERNING EQUATIONS AND TURBULENCE MODEL

In the present development, the density weighted averaging attributed to Favre[10] is used. This decomposition has advantages in flow computations with variable density [see Jones[11]]. Specifically, the averaged governing equations are of simpler form and the physical interpretation of terms in the equations is clearer than when conventional time averaging is used. Reynolds (time) averaging, defined for a scalar, ϕ, as

$$\phi = \bar{\phi} + \phi' \quad , \text{where } \bar{\phi} = \lim_{T\to\infty} \frac{1}{T}\int_{t_o}^{t_o+T} \phi \, dt \quad , \tag{1}$$

is used for pressure, density, molecular stress tensor and molecular heat flux vector. Favre (density) averaging, defined for scalar, ϕ, as

$$\phi = \tilde{\phi} + \phi'' \quad , \text{where } \tilde{\phi} = \frac{\overline{\rho\phi}}{\bar{\rho}} \quad , \tag{2}$$

is used for velocity components, internal energy, turbulent kinetic energy and turbulent energy dissipation rate.

The resulting density averaged two-dimensional Navier-Stokes equations can be written in conservative form in generalized body fitted coordinates as :

$$\frac{\partial \hat{Q}}{\partial t} + \left(\frac{\partial \hat{E}_c}{\partial \xi} + \frac{\partial \hat{F}_c}{\partial \eta}\right) = \left(\frac{\partial \hat{E}_v}{\partial \xi} + \frac{\partial \hat{F}_v}{\partial \eta}\right) + \hat{S} \quad , \tag{3}$$

where

$$\hat{Q} = \frac{1}{J}\begin{pmatrix} \overline{\rho} \\ \overline{\rho}\widetilde{u} \\ \overline{\rho}\widetilde{v} \\ \overline{\rho}\widetilde{e_o} \end{pmatrix}, \quad \hat{E}_c = \frac{1}{J}\begin{pmatrix} \overline{\rho}\widetilde{U} \\ \overline{\rho}\widetilde{u}\widetilde{U}+\xi_x\overline{p} \\ \overline{\rho}\widetilde{v}\widetilde{U}+\xi_y\overline{p} \\ (\overline{\rho}\widetilde{e_o}+\overline{p})\widetilde{U} \end{pmatrix}, \quad \hat{F}_c = \frac{1}{J}\begin{pmatrix} \overline{\rho}\widetilde{V} \\ \overline{\rho}\widetilde{u}\widetilde{V}+\eta_x\overline{p} \\ \overline{\rho}\widetilde{v}\widetilde{V}+\eta_y\overline{p} \\ (\overline{\rho}\widetilde{e_o}+\overline{p})\widetilde{V} \end{pmatrix},$$

$$\hat{E}_v = \frac{1}{J}\begin{pmatrix} 0 \\ \xi_x\tau_{xx}+\xi_y\tau_{yx} \\ \xi_x\tau_{xy}+\xi_y\tau_{yy} \\ \xi_x(\widetilde{u}\tau_{xx}+\widetilde{v}\tau_{xy}-q_x)+\xi_y(\widetilde{u}\tau_{yx}+\widetilde{v}\tau_{yy}-q_y) \end{pmatrix}, \qquad (4)$$

$$\hat{F}_v = \frac{1}{J}\begin{pmatrix} 0 \\ \eta_x\tau_{xx}+\eta_y\tau_{yx} \\ \eta_x\tau_{xy}+\eta_y\tau_{yy} \\ \eta_x(\widetilde{u}\tau_{xx}+\widetilde{v}\tau_{xy}-q_x)+\eta_y(\widetilde{u}\tau_{yx}+\widetilde{v}\tau_{yy}-q_y) \end{pmatrix},$$

$$\hat{S} = \begin{pmatrix} 0 \\ 0 \\ 0 \\ 0 \end{pmatrix}.$$

The metric terms based on a standard coordinate transformation (x,y) --> (ξ,η) are given by

$$\xi_x=\frac{\partial\xi}{\partial x}, \quad \xi_y=\frac{\partial\xi}{\partial y}, \quad \eta_x=\frac{\partial\eta}{\partial x}, \quad \eta_y=\frac{\partial\eta}{\partial y},$$

$$J = \xi_x\eta_y - \eta_x\xi_y \; . \qquad (5)$$

The Jacobian, J, at each gridpoint is equal to 1/(average area of adjacent cells). The contravariant velocity components are given by

$$\widetilde{U} = \xi_x\widetilde{u} + \xi_y\widetilde{v}, \quad \widetilde{V} = \eta_x\widetilde{u} + \eta_y\widetilde{v} \; . \qquad (6)$$

Incorporating an eddy viscosity formulation, the effective stress tensor and the effective heat flux vector are given in cartesian coordinates by :

$$\tau_{ij} = \tau_{lij} - \overline{\rho u_i'' u_j''} = (\mu_l + \mu_t)\left[\left(\frac{\partial\widetilde{u}_i}{\partial x_j} + \frac{\partial\widetilde{u}_j}{\partial x_i}\right) - \frac{2}{3}\delta_{ij}\frac{\partial\widetilde{u}_k}{\partial x_k}\right] - \frac{2}{3}\delta_{ij}\overline{\rho}\widetilde{k},$$

$$q_i = -k\frac{\partial \overline{T}}{\partial x_i} + \overline{\rho u_i'' e''} = -c_p\left(\frac{\mu_l}{Pr_l} + \frac{\mu_t}{Pr_t}\right)\frac{\partial \widetilde{T}}{\partial x_i} \quad . \tag{7}$$

In the derivation of Equations 4 and 7, it has been assumed that the time averaged molecular stress tensor and the molecular heat flux vector are equivalent to their density averaged values. This approximation should be a good one since, compared to turbulent diffusion, molecular diffusion is only significant near solid boundaries, where local Mach number and hence density fluctuations are small. The apparent heat flux vector has been modelled by incorporating the gradient diffusion hypothesis. The laminar Prandtl number, Pr_l, is set to 0.72 for air. The turbulent Prandtl number, Pr_t, is set to the standard value of 0.90.

In the present work, the density averaged k-ε equations are numerically decoupled from the density averaged mean flow equations. Specifically, at each iteration, the four mean flow equations are updated using "frozen" values of eddy viscosity and turbulent kinetic energy from the previous iteration. Likewise, the coupled k-ε equations are then updated using the "frozen" mean flow quantities just computed.

Low Reynolds number forms of the compressible k-ε equations can be written in the same form as Equation 3 where the scaled variable vectors become :

$$\hat{Q} = \frac{1}{J}\begin{pmatrix} \overline{\rho}\,\widetilde{k} \\ \overline{\rho}\,\widetilde{\varepsilon} \end{pmatrix} \quad , \quad \hat{E}_c = \frac{1}{J}\begin{pmatrix} \overline{\rho}\,\widetilde{k}\widetilde{U} \\ \overline{\rho}\,\widetilde{\varepsilon}\widetilde{U} \end{pmatrix} \quad , \quad \hat{F}_c = \frac{1}{J}\begin{pmatrix} \overline{\rho}\,\widetilde{k}\widetilde{V} \\ \overline{\rho}\,\widetilde{\varepsilon}\widetilde{V} \end{pmatrix} \quad ,$$

$$\hat{E}_v = \frac{1}{J}\begin{pmatrix} \left[\mu_l + \frac{\mu_t}{Pr_k}\right]\left[(\nabla\xi\cdot\nabla\xi)\frac{\partial \widetilde{k}}{\partial\xi} + (\nabla\xi\cdot\nabla\eta)\frac{\partial \widetilde{k}}{\partial\eta}\right] \\ \left[\mu_l + \frac{\mu_t}{Pr_\varepsilon}\right]\left[(\nabla\xi\cdot\nabla\xi)\frac{\partial \widetilde{\varepsilon}}{\partial\xi} + (\nabla\xi\cdot\nabla\eta)\frac{\partial \widetilde{\varepsilon}}{\partial\eta}\right] \end{pmatrix} \quad , \tag{8}$$

$$\hat{F}_v = \frac{1}{J}\begin{pmatrix} \left[\mu_l + \frac{\mu_t}{Pr_k}\right]\left[(\nabla\eta\cdot\nabla\xi)\frac{\partial \widetilde{k}}{\partial\xi} + (\nabla\eta\cdot\nabla\eta)\frac{\partial \widetilde{k}}{\partial\eta}\right] \\ \left[\mu_l + \frac{\mu_t}{Pr_\varepsilon}\right]\left[(\nabla\eta\cdot\nabla\xi)\frac{\partial \widetilde{\varepsilon}}{\partial\xi} + (\nabla\eta\cdot\nabla\eta)\frac{\partial \widetilde{\varepsilon}}{\partial\eta}\right] \end{pmatrix} \quad ,$$

$$\hat{S} = \frac{1}{J}\begin{pmatrix} P - \overline{\rho}\tilde{\varepsilon} + D \\ \left(C_1 f_1 P - C_2 f_2 \overline{\rho}\tilde{\varepsilon}\right)\frac{\tilde{\varepsilon}}{\tilde{k}} + E \end{pmatrix} ,$$

where the production term P is given in cartesian coordinates as

$$\begin{aligned} P = &\left\{2\mu_t \frac{\partial \tilde{u}}{\partial x} - \left[\frac{2}{3}\overline{\rho}\,\tilde{k} + \mu_t\left(\frac{\partial \tilde{u}}{\partial x} + \frac{\partial \tilde{v}}{\partial y}\right)\right]\right\}\frac{\partial \tilde{u}}{\partial x} \\ &+ \left\{2\mu_t \frac{\partial \tilde{v}}{\partial y} - \left[\frac{2}{3}\overline{\rho}\,\tilde{k} + \mu_t\left(\frac{\partial \tilde{u}}{\partial x} + \frac{\partial \tilde{v}}{\partial y}\right)\right]\right\}\frac{\partial \tilde{v}}{\partial y} \\ &+ \mu_t\left(\frac{\partial \tilde{u}}{\partial y} + \frac{\partial \tilde{v}}{\partial x}\right)^2 \end{aligned} . \qquad (9)$$

The mass averaged turbulent kinetic energy and isotropic component of turbulent kinetic energy dissipation rate are defined as

$$\tilde{k} = \frac{\frac{1}{2}\overline{\rho u_i'' u_i''}}{\overline{\rho}} , \quad \tilde{\varepsilon} = \frac{\overline{\nu\rho \frac{\partial u_i''}{\partial x_j}\frac{\partial u_i''}{\partial x_j}}}{\overline{\rho}} . \qquad (10)$$

The eddy viscosity is obtained from

$$\mu_t = \frac{C_\mu f_\mu \overline{\rho}\,\tilde{k}^2}{\tilde{\varepsilon}} . \qquad (11)$$

The particular form of low Reynolds number model used in the code was originally devised by Chien for incompressible flow[12]. Compressible forms have been given by Coakley[13] and more recently by Nichols[14]. For this model, the constants and functions in Equations 8 through 11 are given by

$$f_\mu = 1 - \exp(-.0115y^+) , f_1 = 1 , f_2 = 1 - \frac{2}{9}\exp(-R_T^2/36) ,$$

$$R_T = \frac{\overline{\rho}\,\tilde{k}^2}{\mu_l \tilde{\varepsilon}} , y^+ = \frac{\overline{\rho} n u^*}{\mu_l} , u^* = \sqrt{\frac{\tau_w}{\overline{\rho}}} , \qquad (12)$$

$$\mathcal{D} = -\frac{2\mu_l \tilde{k}}{n^2}, \mathcal{E} = -\frac{2\mu_l \tilde{\varepsilon}}{n^2} \exp(-.5y^+) \quad ,$$

$$C_\mu = 0.09 \; , \; C_1 = 1.35 \; , \; C_2 = 1.80 \; , \; Pr_k = 1.0 \; , \; Pr_\varepsilon = 1.3 \quad .$$

Following Hobson[15], the blade normal coordinate, n, in Equations 12, is replaced by absolute distance from leading and trailing edge, upstream and downstream of the passage respectively.

The transport variable, ε, used in this model is the isotropic component of the dissipation rate, though the ε equation is derived for the total dissipation rate. As discussed by Jones[16], at high local Reynolds numbers, the anisotropic component of dissipation is negligible, so the model remains valid in these regions. Near a solid wall, however, the anisotropic dissipation component is not negligible, and the isotropic component, ε, goes to zero. The term, $\mathcal{D}$, accounts for the non-zero value of total dissipation near the wall, so that the model also remains valid near solid walls and retains the convenience of specifying the $\varepsilon = 0$ boundary condition there.

It should be noted, that although the k-ε equations have been cast in compressible form, the modelling assumptions invoked here are essentially those for incompressible flow. Specifically, terms in the unmodelled k and ε equations which contain density fluctuation terms, ρ', are neglected. Also, pressure diffusion terms are neglected.

No thin layer approximations are made in either the mean flow or turbulence transport equations.

NUMERICAL SOLUTION

Discretization

The H-grid flow solver used in the present studies incorporates a standard 4-stage Runge-Kutta scheme as first applied to Euler calculations by Jameson, Schmidt and Turkel[1],

$$\begin{aligned}
\hat{Q}^1 &= \hat{Q}^n + \frac{1}{4}\Delta t\, \hat{R}(\hat{Q}^n) \\
\hat{Q}^2 &= \hat{Q}^n + \frac{1}{3}\Delta t\, \hat{R}(\hat{Q}^1) \\
\hat{Q}^3 &= \hat{Q}^n + \frac{1}{2}\Delta t\, \hat{R}(\hat{Q}^2) \\
\hat{Q}^{n+1} &= \hat{Q}^n + \Delta t\, \hat{R}(\hat{Q}^3) \quad .
\end{aligned} \tag{13}$$

Here, the residual, $\hat{R}$, is defined according to

$$\hat{R} = -\left(\frac{\partial \hat{E}_c}{\partial \xi} + \frac{\partial \hat{F}_c}{\partial \eta}\right) + \left(\frac{\partial \hat{E}_v}{\partial \xi} + \frac{\partial \hat{F}_v}{\partial \eta}\right) + \hat{S} \quad . \tag{14}$$

The scheme is fourth order accurate in time. Second order accurate central differences are used to discretize the derivatives in Equation 14. Viscous and source terms are evaluated prior to the first stage, convective terms are computed at every stage. The stability region for the scheme is shown in Figure 1.

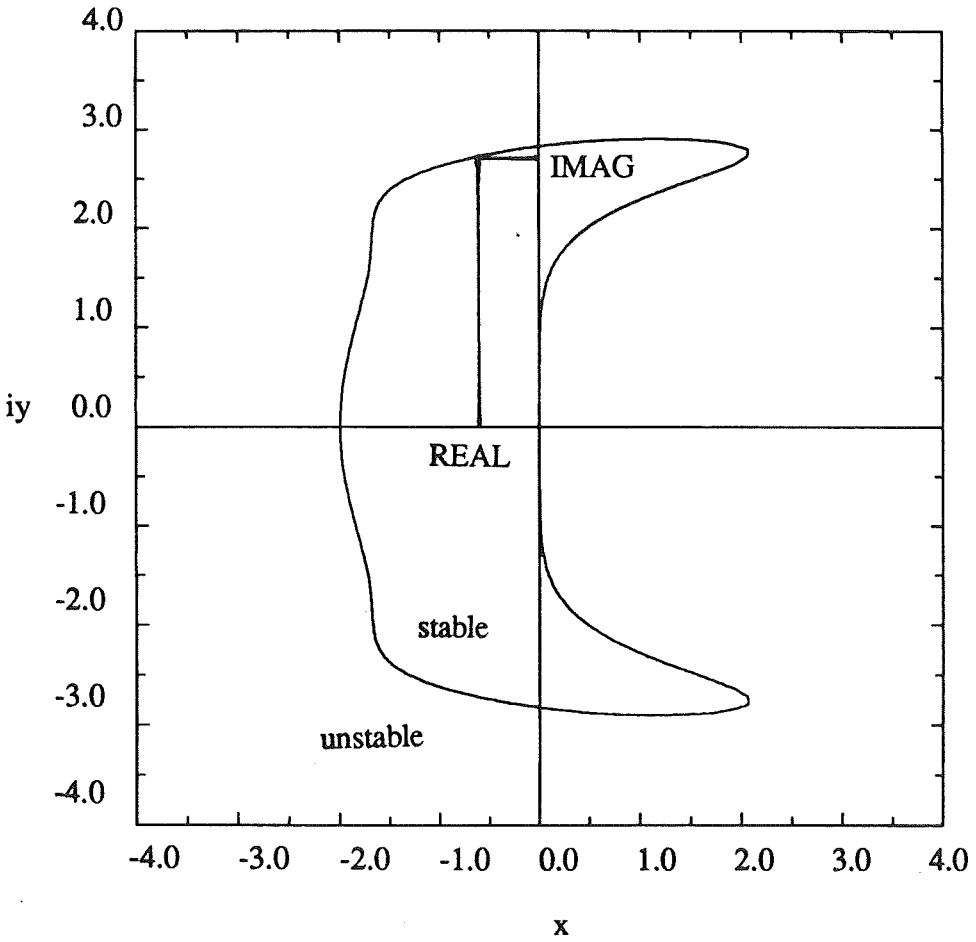

Figure 1. Stability region for standard 4-stage scheme.

The curve in Figure 1 represents the contour $|g(z)| = 1.0$, where z is the complex fourier symbol of a discretized scalar convection-diffusion equation at a particular wavenumber, and g is the amplification factor arising from a 1-D scalar VonNeumann linear stability analysis of the given scheme applied to this discretized equation.

The differencing molecule used to discretize the flux vectors in computational space is shown in Figure 2. Flux vectors, $\hat{E}$ and $\hat{F}$, are computed at mid-points between nodes. For viscous fluxes, this scheme incorporates information from all nine points in the differencing molecule. This approach requires three times the storage for metric terms than if viscous fluxes were computed on the grid vertices themselves (13 point molecule). However, the truncation error associated with discretizing the viscous fluxes on a uniform cartesian mesh using a thirteen point scheme is $O(4\Delta x^{2)} + O(4\Delta y^{2)}$ as compared to $O(\Delta x^{2)} + O(\Delta y^{2)}$ for the nine point molecule, consistent with the truncation error of the convective fluxes. It is also easier to apply periodic and wall-function boundary conditions with the more compact differencing molecule.

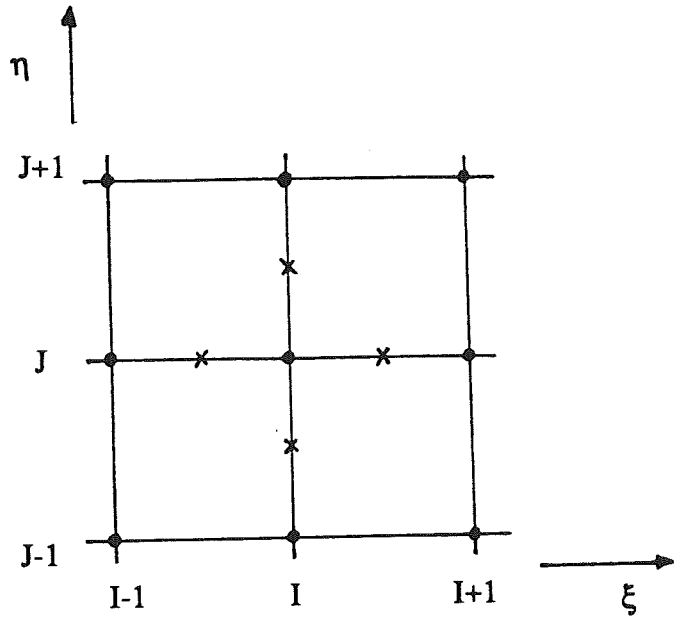

Figure 2. Computational molecule and index convention for the present scheme. Flux vectors computed at midpoints (marked x) between vertices.

To accelerate the solution to steady state, locally varying timesteps are computed based on a linear stability analysis of the discretized Navier-Stokes equations. The resulting timestep specification is given as :

$$\Delta t = \text{MIN}\left[\Delta t_c, \Delta t_v\right] = \text{MIN}\left[\frac{\text{IMAG}}{|\tilde{U}| + |\tilde{V}| + a\sqrt{(\nabla\xi\cdot\nabla\xi)+(\nabla\eta\cdot\nabla\eta)+|2(\nabla\xi\cdot\nabla\eta)|}}, \frac{\text{REAL}}{\frac{4\gamma}{\tilde{\rho}}\left(\frac{\mu_l}{Pr_l}+\frac{\mu_t}{Pr_t}\right)\left[(\nabla\xi\cdot\nabla\xi)+(\nabla\eta\cdot\nabla\eta)\right]+\frac{4}{3\tilde{\rho}}(\mu_l+\mu_t)\left[7|\nabla\xi\cdot\nabla\eta|+\sqrt{(\nabla\xi\cdot\nabla\xi)(\nabla\eta\cdot\nabla\eta)}\right]}\right] \quad . \quad (15)$$

Here, IMAG and REAL are input parameters corresponding to operational CFL and VonNeumann numbers chosen to ensure stability (see Figure 1). A similar expression is given by Martinelli [17]. The first term in the brackets in Equation 15 arises from the convection operators, the latter term corresponds to physical viscous terms. Note that for the present uncoupled approach, the turbulent kinetic energy does not appear in the stablility expressions.

For large Reynolds number flows, the H-grids used must be highly stretched in the pitchwise direction, in order to adequately resolve near-wall gradients. Consequently, the metric terms, η_x, η_y in Equation 15 can become very large near the J = 1 and J = NJ boundaries. Also, when using a two equation turbulence model, as in the present study, the eddy viscosity, μ_t, can be very large near the J = 1 and J = NJ boundaries, upstream and downstream of the blades, where wall damping effects are negligible This combination of large eddy viscosity and grid metrics causes the viscous stability term to dominate in these regions, and it has been found that it is crucial to include the influence of these terms in determining a stable local timestep. For the supersonic and subsonic cascade test cases computed herein, $\Delta t_v < \Delta t_c$ for 40.0% and 7.5 % of the grid points at convergence, respectively.

Even for the computation of steady, one-dimensional, inviscid flows, the use of highly stretched grids gives rise to significantly reduced convergence rates in explicit schemes. This affect arises due to characteristic propagation speed in the streamwise direction. In two dimensions an analagous situation arises when the computational mesh is clustered in one curvilinear coordinate direction to resolve regions where flowfield gradients are large. Specifically, the maximum local stable timestep in regions where the mesh is highly clustered in the η direction, is inversely proportional to the metric term, $\sqrt{(\nabla\eta\cdot\nabla\eta)}$, which can be very large. It is the nature of this inviscid effect which often allows one to use a local timestep based solely on inviscid considerations, for viscous flow computations.

The k and ε equations each contain non-linear production and destruction source terms which can be very large near solid boundaries. According to linear stability theory, such terms can also severely reduce convergence rates if a purely explicit scheme is used to discretize the equations. It was found that

by incorporating a composite viscous-inviscid timestep specification, the stability restrictions on the k-ε solution are not much more severe than the restrictions on the mean flow equations discussed above. In fact, it was possible to compute high Reynolds number flows with this turbulence model using a purely explicit treatment in reasonable computation times. A local timestep for the k-ε equations of approximately 1/4 of the stable mean flow timestep was satisfactory for the cascade flows computed herein. Converged solutions were thereby obtained in computation times approximately twice those of solutions using an algebraic eddy viscosity model. This is illustrated for turbulent flat plate flow computations presented in the Results section.

Artificial Dissipation

Central difference schemes applied to hyperbolic equations that do not contain any inherent dissipation require the addition of artificial dissipation, to damp high wave number disturbances. These disturbances can be introduced into linear problems through inconsistent boundary condition treatment or machine roundoff error. In non-linear problems, such disturbances can be introduced through aliasing of sub-grid scale non-linear disturbances, to lower, resolvable wave numbers. Even for viscous flow calculations, artificial dissipation must be introduced into the scheme because the physical viscous terms are only effective in damping frequencies at higher wave numbers than can be resolved on practical grids.

In the present work, artificial dissipation is added to the discretized mean flow equations as

$$\hat{R} = -\left(\frac{\partial \hat{E}_c}{\partial \xi} + \frac{\partial \hat{F}_c}{\partial \eta}\right) + \left(\frac{\partial \hat{E}_v}{\partial \xi} + \frac{\partial \hat{F}_v}{\partial \eta}\right) + D(Q) + \hat{S} \tag{16}$$

Here, D(Q) represents a mixed 2nd and 4th order nonconservative artificial dissipation operator similar to that devised by Jameson, Schmidt and Turkel[1].

$$\begin{aligned} D(Q) &= D_\xi(Q) + D_\eta(Q)\,, \\ D_\xi(Q) &= S_{2\xi}\delta_{\xi\xi}Q + S_{4\xi}\delta_{\xi\xi\xi\xi}Q\,, \\ D_\eta(Q) &= S_{2\eta}\delta_{\eta\eta}Q + S_{4\eta}\delta_{\eta\eta\eta\eta}Q\,. \end{aligned} \tag{17}$$

The fourth order operators are included to damp high wave number errors and the second order operators are included to improve shock capturing.

As pointed out by Pulliam[18], artificial dissipation terms should operate on physical values of the flowfield variables and as such must be appropriately scaled by the metric Jacobian. Artificial dissipation terms must also be scaled by the local timestep to ensure that the steady state solution is independent of the timestep. In addition to the above consistency requirements on the dissipation scaling, levels of dissipation should always be reduced to levels adequate to stabilize a scheme without altering the accuracy of the solution. For the computation of viscous flows on highly stretched grids, this latter requirement is a sensitive matter.

For high Reynolds number flows, very highly stretched grids must be used to resolve body normal gradients in near wall regions. If the artificial dissipation terms in both the ξ and η directions are scaled by the local timestep, on grids which are highly stretched in the η direction, excessive dissipation is introduced in the ξ direction. This effect is discussed by Caughey and Turkel[19] and Swanson and Turkel[20]. This excessive dissipation may reduce accuracy and convergence rates in viscous flow computations. A recently devised eigenvalue scaling of the artificial dissipation terms, due to Martinelli[17] alleviates this problem. Since the present technique is primarily used to compute viscous flows on highly stretched grids, anisotropic dissipation scaling factors similar to those used by Martinelli are incorporated. $S_{2\xi}$, $S_{2\eta}$, $S_{4\xi}$, $S_{4\eta}$ in Equation 17 are defined

$$S_{2\xi} = \frac{\sigma_{2\xi}}{J}\left[\frac{1}{\Delta t_{c\xi}}\left(1+\frac{\Delta t_{c\xi}}{\Delta t_{c\eta}}\right)^{\alpha}\right],\ S_{2\eta} = \frac{\sigma_{2\eta}}{J}\left[\frac{1}{\Delta t_{c\eta}}\left(1+\frac{\Delta t_{c\eta}}{\Delta t_{c\xi}}\right)^{\alpha}\right],$$
$$S_{4\xi} = \frac{\sigma_{4\xi}}{J}\left[\frac{1}{\Delta t_{c\xi}}\left(1+\frac{\Delta t_{c\xi}}{\Delta t_{c\eta}}\right)^{\alpha}\right],\ S_{4\eta} = \frac{\sigma_{4\eta}}{J}\left[\frac{1}{\Delta t_{c\eta}}\left(1+\frac{\Delta t_{c\eta}}{\Delta t_{c\xi}}\right)^{\alpha}\right]. \tag{18}$$

Here, $\Delta t_{c\xi}$, $\Delta t_{c\eta}$, are timesteps corresponding to unit CFL limit for the inviscid one-dimensional problem in each direction,

$$\Delta t_{c\xi} = \frac{1}{|\tilde{U}| + a\sqrt{(\nabla\xi\cdot\nabla\xi)}},\ \Delta t_{c\eta} = \frac{1}{|\tilde{V}| + a\sqrt{(\nabla\eta\cdot\nabla\eta)}}. \tag{19}$$

The choice of unit CFL scaling in the numerator of Equation 19 ensures that the steady state solution will be independent of the operational CFL limit used to compute local timesteps. If $\alpha = 1$, Equation 18 reduces to standard isotropic scaling. As mentioned above, this introduces excessive dissipation in the ξ direction in regions where the grid is stretched in the η direction. If $\alpha = 0$, the scaling becomes purely anisotropic. If the grid is very highly stretched in the η direction, such scaling may not provide enough dissipation in the ξ direction, resulting in reduced convergence rates. For intermediate values of α

between 1/2 and 2/3, Martinelli[17], Swanson and Turkel[20] and Radespiel and Swanson[21] have shown good convergence rates for Euler and Navier-Stokes calculations on highly clustered grids.

Another scaling issue is important in the computation of viscous flows. All of the mean flow equations with the exception of the continuity equation contain physical dissipation terms. Also, near solid boundaries, physical dissipation terms in the energy equation are quite small, in the absence of heat transfer effects. However, near solid boundaries, the viscous fluxes in the momentum are quite large and are themselves adequate to provide smoothing. In these same regions, second and fourth derivatives of the transport variables can be quite large leading to large values of artificial dissipation there. This well recognized phenomenon [see Davis, Ni and Carter[22] and Swanson and Turkel [20] for instance] gives rise to very large nonphysical values of total dissipation in the near wall region. Often some sort of geometric decay function is used to control the levels of artificial dissipation in these regions to reduce the magnitude of numerical to physical smoothing to acceptable levels. In the present work, the scaling functions in Equation 18 are multiplied by a normalized square of the local velocity, V^2/V^2_∞, for the momentum equations.

Following Jameson, Schmidt and Turkel[1], the non-linear weighting functions in Equation 18 are determined from

$$\begin{aligned} \sigma_{2\xi} &= \kappa_2 \, \mathrm{MAX}\left(\nu_{\xi i+1,j}, \nu_{\xi i,j}, \nu_{\xi i-1,j}\right) , \\ \sigma_{4\xi} &= - \, \mathrm{MAX}\left(0, \kappa_4 - \sigma_{2\xi}\right) , \end{aligned} \tag{20}$$

where the monitoring parameters ν, are normalized second derivatives of pressure,

$$\nu_{\xi i,j} = \frac{\left| p_{i+1,j} - 2\, p_{i,j} + p_{i-1,j} \right|}{\left| p_{i+1,j} + 2\, p_{i,j} + p_{i-1,j} \right|} , \tag{21}$$

and $\kappa_2 \cong 1/4$, $\kappa_4 \cong 1/64$. Expressions similar to Equations 20 and 21 are used in the η direction. When shocks are not anticipated in the flowfield, κ_2 is set equal to zero so that the artificial dissipation added to the mean flow is fourth order only.

To examine the effects of the scalings given, two numerical experiments were conducted. The subsonic cascade described below was used as a numerical test bed. The reader is referred to the next section for specifics on this flow configuration.

The first experiment attempted to isolate the influence of eigenvalue scaling on accuracy and convergence. The test case was run for five thousand iterations using the following values of α in Equation 18 : $\alpha = 1$ (standard isotropic scaling), $\alpha = 0$ (purely anisotropic scaling) and $\alpha = 2/3$ (intermediate scaling). In Figure 3, the convergence histories for the three cases are plotted.

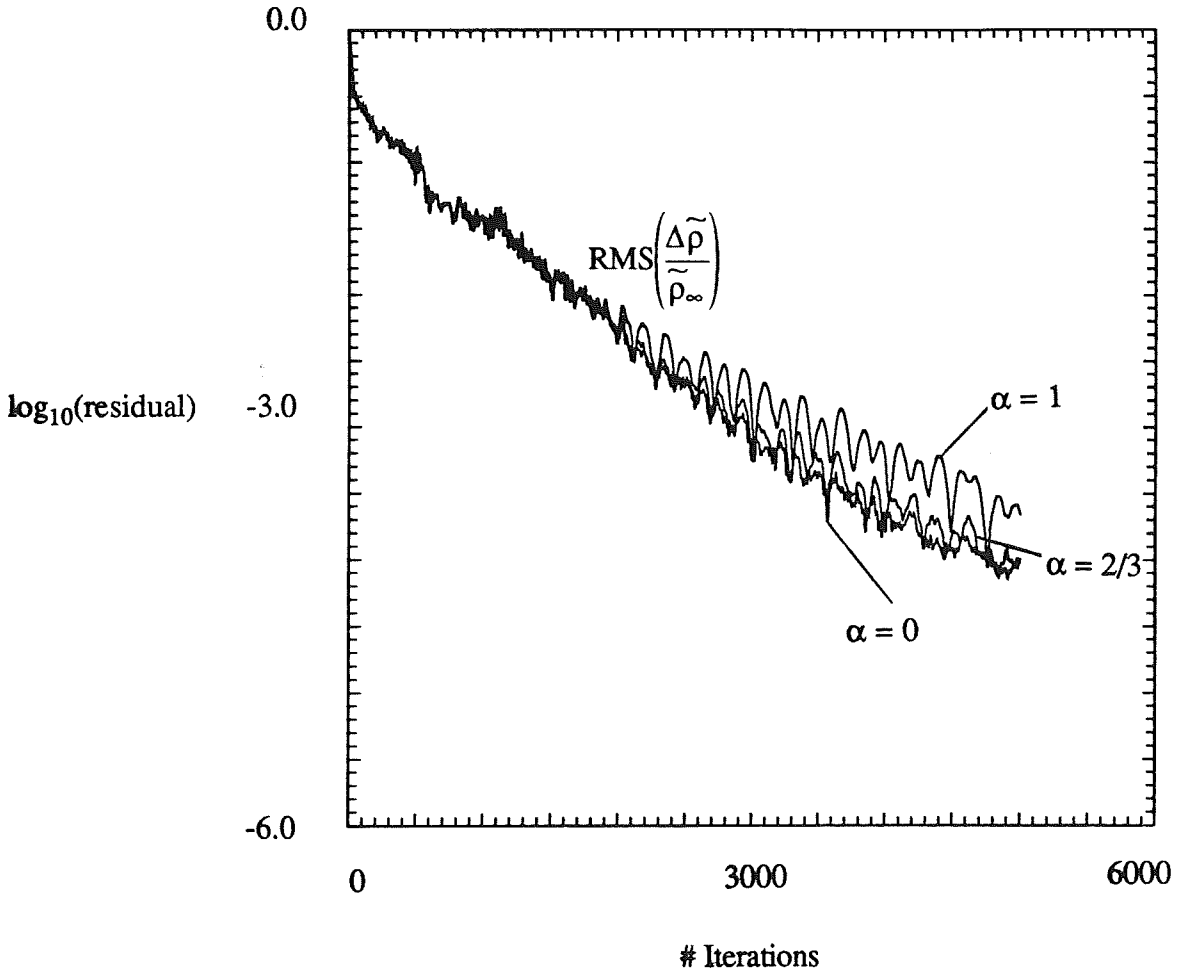

Figure 3. Convergence histories for various eigenvalue scalings.

Scaling the dissipation anisotropically does provide an improved convergence rate for this case as expected. In addition, purely anisotropic scaling provides somewhat superior convergence rate than the weighted scaling ($\alpha = 2/3$). This suggests that, for this case, such scaling does not reduce dissipation in the ξ direction to the point of destabilizing the solution. The influence of these scalings on accuracy was found to be negligible.

The second experiment sought to detect the influence of spurious dissipation levels in near wall boundaries, and to see how the proposed velocity scaling affects solution convergence and accuracy. When the ratio of artificial to physical dissipation terms in Equation 16 were compared, it was found that for this test case, at convergence, artificial dissipation levels were as high as ten times the physical dissipation terms at the first several grid points adjacent to the wall! By incorporating the velocity scaling exactly as proposed above, it was possible to reduce the artificial to physical dissipation ratio to less than .01 in the near wall region, except in the immediate vicinity of the leading and trailing edges. The convergence rates compared very closely, but as shown in Figure 4, the converged solutions showed some discrepancy.

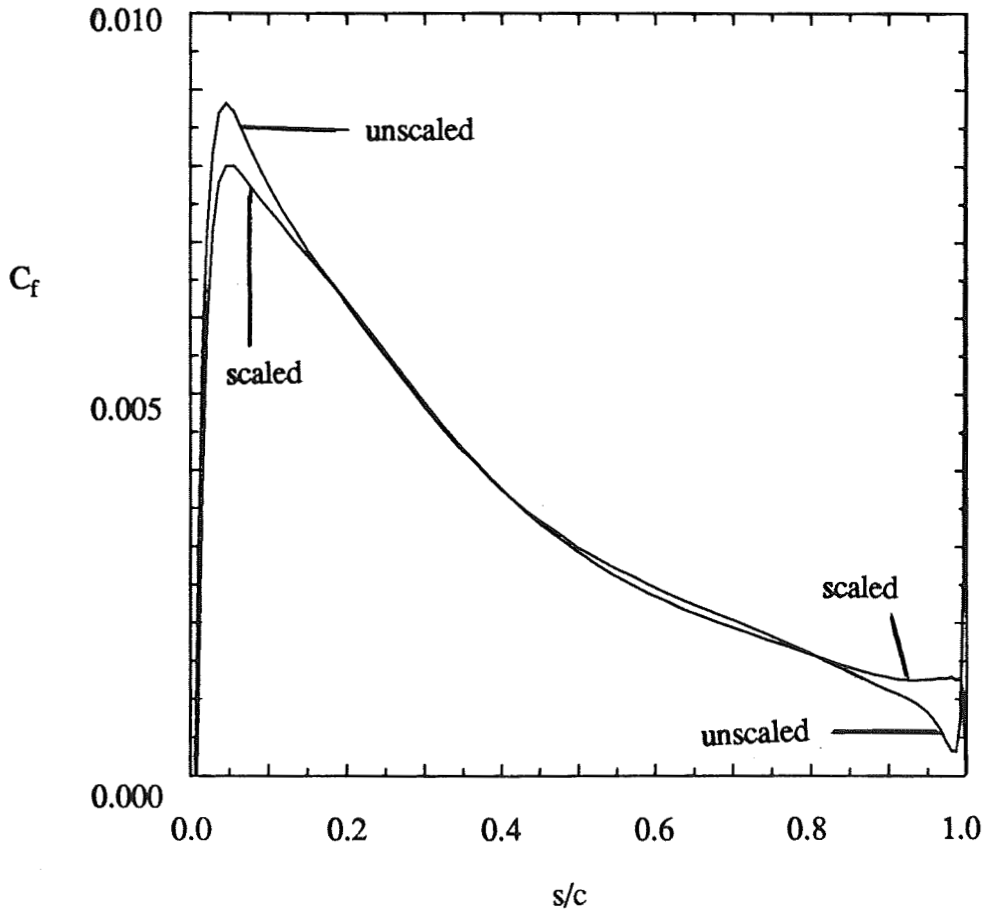

Figure 4. Comparison of predicted skin friction coefficient, along the suction surface of the test cascade, with and without velocity scaling of the artificial dissipation.

It is clear from this figure that unnecessary levels of artificial dissipation in boundary layers can affect solution accuracy in practical application.

Both eigenvalue scaling (with $\alpha = 2/3$) and local velocity scaling were used in all computations that follow.

It is worth noting, that the dissipation scaling considerations addressed here are especially important when a multigrid acceleration scheme is used. Careful tuning of artificial dissipation levels is crucial when performing explicit multigrid calculations on highly stretched grids. This is because inadequate or excessive dissipation can diminish the high wave number damping properties of the driving scheme thereby rendering multigrid acceleration less effective[23].

Lack of adequate grid resolution in the ξ direction just upstream and downstream of the blade edges, causes the wall damping function, f_μ, in Equation 12 to be effective only over two to four grid points in this direction. This gives rise to very large streamwise gradients in k and ε at the leading and trailing edges, which in turn leads to slowly growing oscillations in these variables. It was found necessary to smooth these oscillations by incorporating small amounts of second order artificial dissipation in the k and ε equations in a manner consistent with Equations 16 and 17, with $S_{2\xi} = S_{2\eta} \cong 0.002$, $S_{4\xi} = S_{4\xi} = 0.0$.

Boundary and Initial Conditions

Along blade surfaces the no-slip condition is imposed upon the velocities, pressure is extrapolated from adjacent grid points, and density is computed based on specified wall temperature or heat transfer rate. At the inlet, total pressure and total temperature are specified. For subsonic inflow, either inlet flow angle or pitchwise velocity are specified, and the R^- characteristic is extrapolated along η = constant grid lines from the interior of the computational domain. At subsonic outflow boundaries, static pressure is specified and velocity components and entropy are extrapolated along η = constant grid lines. Along periodic boundaries, cyclic information is used when discretizing derivatives in the η direction.

Constant values of k and ε are imposed at the inflow boundary based on specified freestream turbulence intensity and length scale,

$$T_{u\infty} = \frac{\sqrt{\frac{2}{3}\tilde{k}_\infty}}{\tilde{V}_\infty}, \qquad (19)$$

$$L_\infty = \frac{C_\mu \tilde{k}^{3/2}}{\tilde{\varepsilon}}.$$

C-3

Typically , the freestream length scale is set between .001 and .01 times the pitch of the blade passage. At the outflow boundary, values of k and ε are extrapolated along η = constant grid lines from the interior of the computational domain. Turbulent kinetic energy and isotropic dissipation rate are set to zero along solid boundaries, as discussed in the turbulence model section.

The flowfield is initialized using standard quasi-1D analysis to provide uniform initial velocity profiles along each ξ = constant grid line. This gives rise to huge production terms in the k-ε equations, and can cause solutions to become rapidly unstable. This problem is alleviated by running the code in laminar mode for a couple hundred iterations to develop a slight boundary layer, thereby reducing the size of these terms.

RESULTS AND DISCUSSION

Computational Considerations

The code has been validated for laminar and turbulent flat plate boundary layer flows, where nearly exact agreement with theory and experiment were obtained. In addition, it has been applied to laminar flow about a circular arc bump in a channel, as well as to turbulent flow about a similar configuration with a heated wall using an algebraic eddy viscosity model. These two model problems had been computed by Chima and Johnson[24] and Davis, Ni and Carter[22] respectively. The present method yielded nearly exact agreement with these two sets of results. Implicit residual smoothing is available to accelerate the convergence to steady state of the mean flow. However, successful implementation of implicit smoothing for the turbululence transport equations has not been realized. For consistency, then, residual smoothing was not used in obtaining any of the proceeding results.

For turbulent flow calculations, the highly vectorized code executes at 2.8×10^{-5} CPU seconds / (gridpoint * iteration) on the Cray Y-MP 8/32 at the Pittsburgh Supercomputer Center. When an algebraic eddy viscosity model is used, the execution rate is 1.7×10^{-5} CPU seconds / (gridpoint * iteration). Since the same near wall resolution is needed for these two models, similar grids must be used. Experience with the code has shown that mean density residual converges slightly more slowly when using the k-ε model, so the total overhead associated with using the higher order model is less than a factor of 2.0.

To illustrate the above considerations, convergence histories are presented here for the prediction of developing turbulent flow over a flat plate. Both the algebraic eddy viscosity model due to Baldwin and Lomax[25] and the present two-equation model were used.

Both cases converged very slowly due to the extremely high aspect ratio of the grid (1.2×10^4 at the trailing edge of the plate). The convergence history for the computations is shown in Figure 5. It took approximately 10000 iterations for both calculations to converge to within engineering accuracy (taken to be a 4.5 order of magnitude drop in the RMS density residual). Note that the convergence rates are similar. This illustrates that it is primarily "inviscid" stablity constraints, and not the stiffness associated with large source terms in the turbulence transport equations, which give rise to the slower convergence rates which occur when explicit schemes are used to compute turbulent flows on highly stretched meshes.

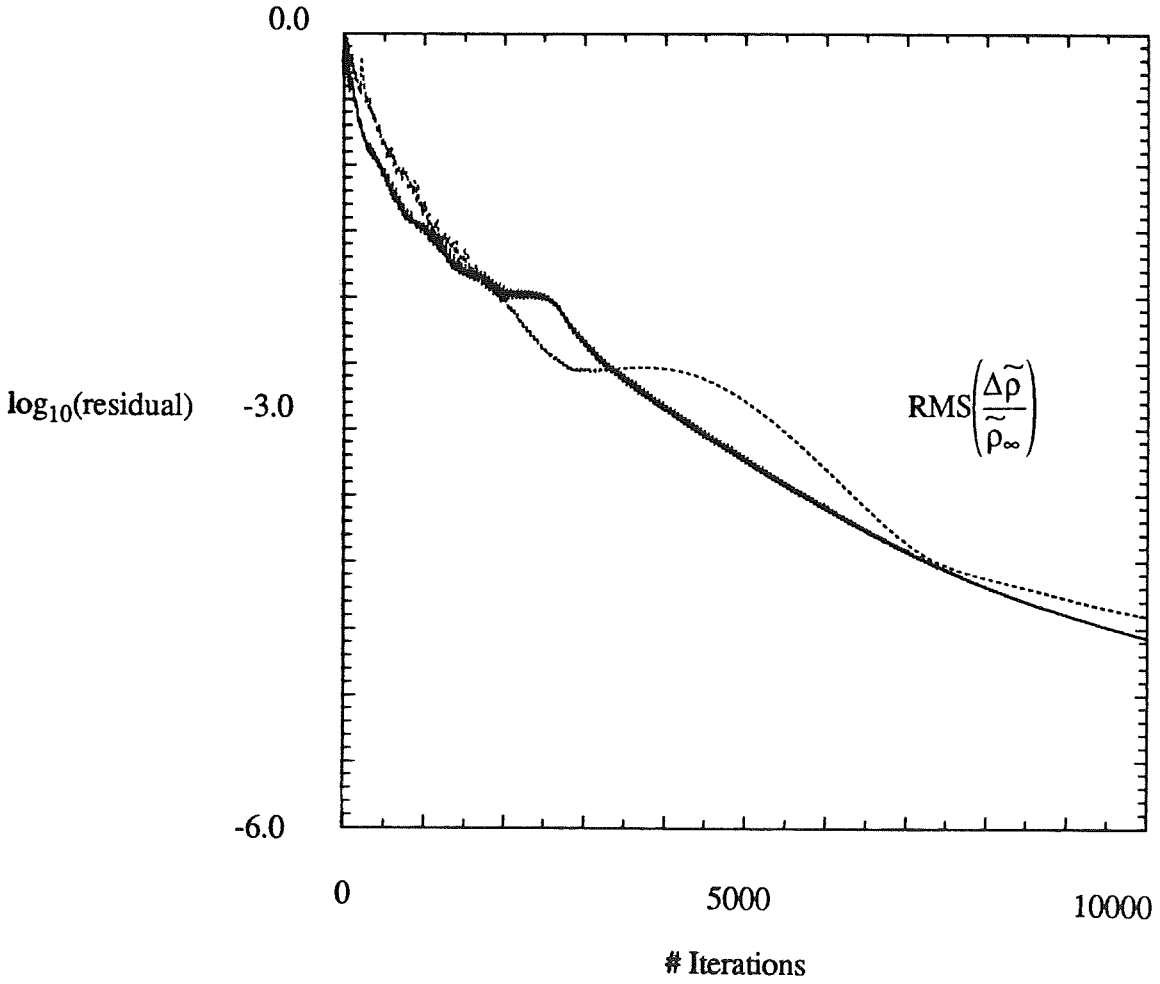

Figure 5. Convergence history for turbulent flat plate boundary layer calculations (solid line = Baldwin and Lomax, dashed line = k-ε).

DFVLR PAV-1.5 Supersonic Compressor Cascade

The first cascade to be investigated is the PAV-1.5 supersonic compressor cascade tested at DFVLR by Schreiber[26]. This pre-compression blade was designed especially to investigate shock-boundary layer interaction with separation. At the test freestream Mach number, a standoff leading edge shock forms, which gives rise to a separated shock-boundary layer interaction aft of mid chord on the suction surface of the adjacent passage. Though the measured absolute inlet Mach number was supersonic, the blade row stagger angle was high so the axial component of the inlet velocity was subsonic. This gives rise to the "unique incidence" condition wherein there exists a fixed relationship between inlet Mach number and inlet flow angle. Beyond a critical Mach number this condition exists and inlet conditions become independent of back pressure. This phenomena as well as the complex wave interaction field within the passage and shock-boundary-layer interaction provide a challenging test case for both numerical scheme and turbulence model.

The computed case was experimentally tested in air at an inlet Mach number of 1.53 and a maximum attainable static pressure ratio of 2.13. The measured axial velocity density ratio of 1.02 indicates that the flow was close to two-dimensional. The Reynolds number based on chord was 2.7×10^6. The inlet turbulence intensity was measured using a Laser-two-focus (L2F) velocimeter to be no more than 1 %, which is the value used in the computations. As mentioned above, the inlet Mach number is supersonic, but axial velocity at the inlet to the computational domain is subsonic allowing left running characteristics to propagate out of the inlet plane. For this reason, subsonic inlet boundary conditions were specified : $p_o = 101325$ N/m^2, $T_o = 300$ K, $V_{\theta\infty} = 379.5$ m/s^2. At the subsonic exit plane the backpressure, $p_e =$ 56500 N/m^2, was specified corresponding to the experimentally measured pressure ratio of the cascade, $p_2/p_1 = 2.13$.

The 129 x 100 computational mesh used was generated using Sorenson's[27] GRAPE code, modified by Gorski[28] to generate H-grids, and is shown in Figure 6. The blade normal grid spacing at the wall was prescribed as .000011 chord. This yielded values of $y^+ \leq 1$ at grid points adjacent to the walls. Except in the immediate vicinity of the leading and trailing edges, the suction and pressure surface boundary layers had at least 9 grid points with values of $y^+ \leq 20$.

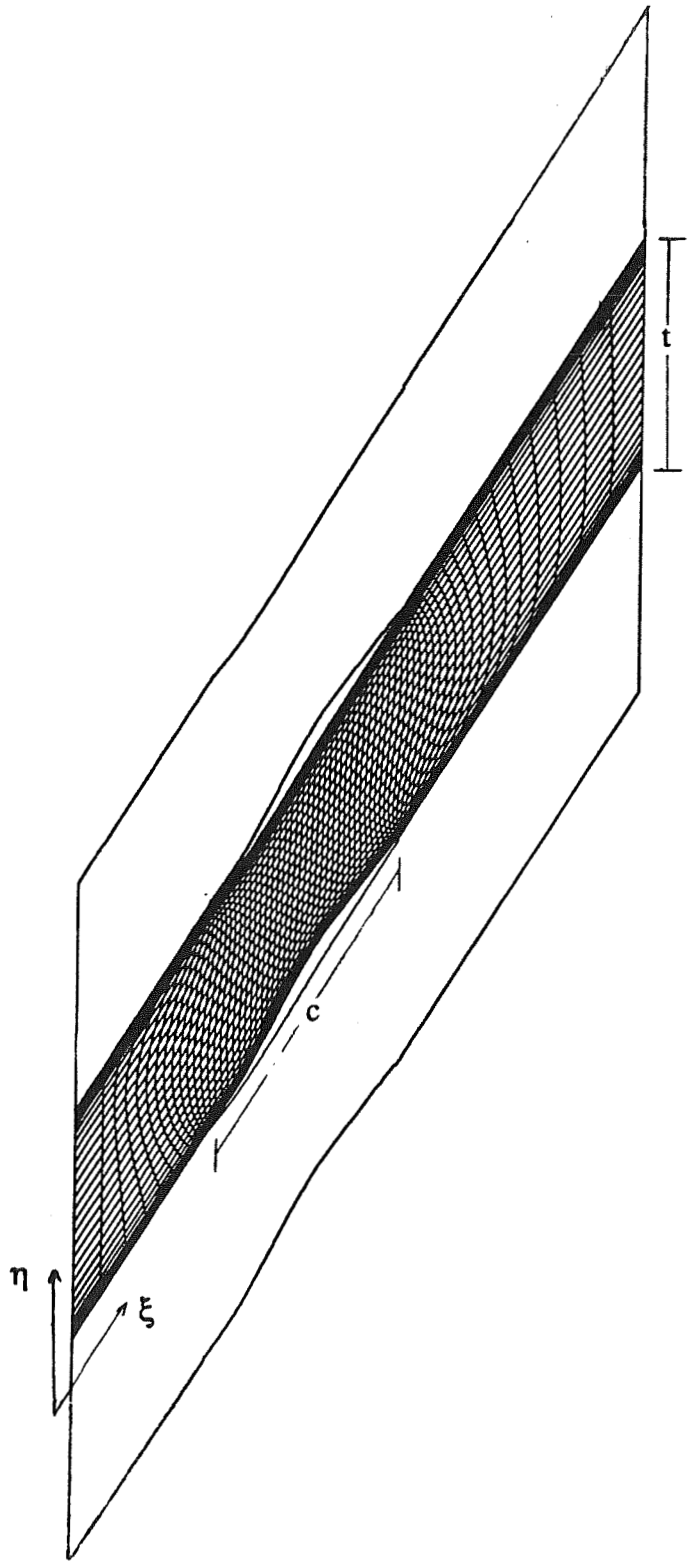

Figure 6. 129 x 100 computational grid for the PAV-1.5 cascade.
For clarity, only every other grid line is shown in both ξ and η directions.

The convergence history for this computation is shown in Figure 7. It took approximately 6500 iterations for this calculation to converge within engineering accuracy as measured by the invariance of total number of supersonic gridpoints in the field. This corresponded to approximately 39 minutes of CPU time on the Pittsburgh Cray. It was not possible to "cold start" the initialized flowfield at the specified pressure ratio, as the code became rapidly unstable when this was attempted. Rather, the back pressure had to be increased in a stepwise fashion with iteration (notice "jumps" in convergence at iteration 500, 1000, 2000), until the experimentally imposed pressure ratio could be specified at iteration 2000. It is felt that the "unhealthy" convergence history is due in part to the highly clustered grid and also to the nearly choked operating condition.

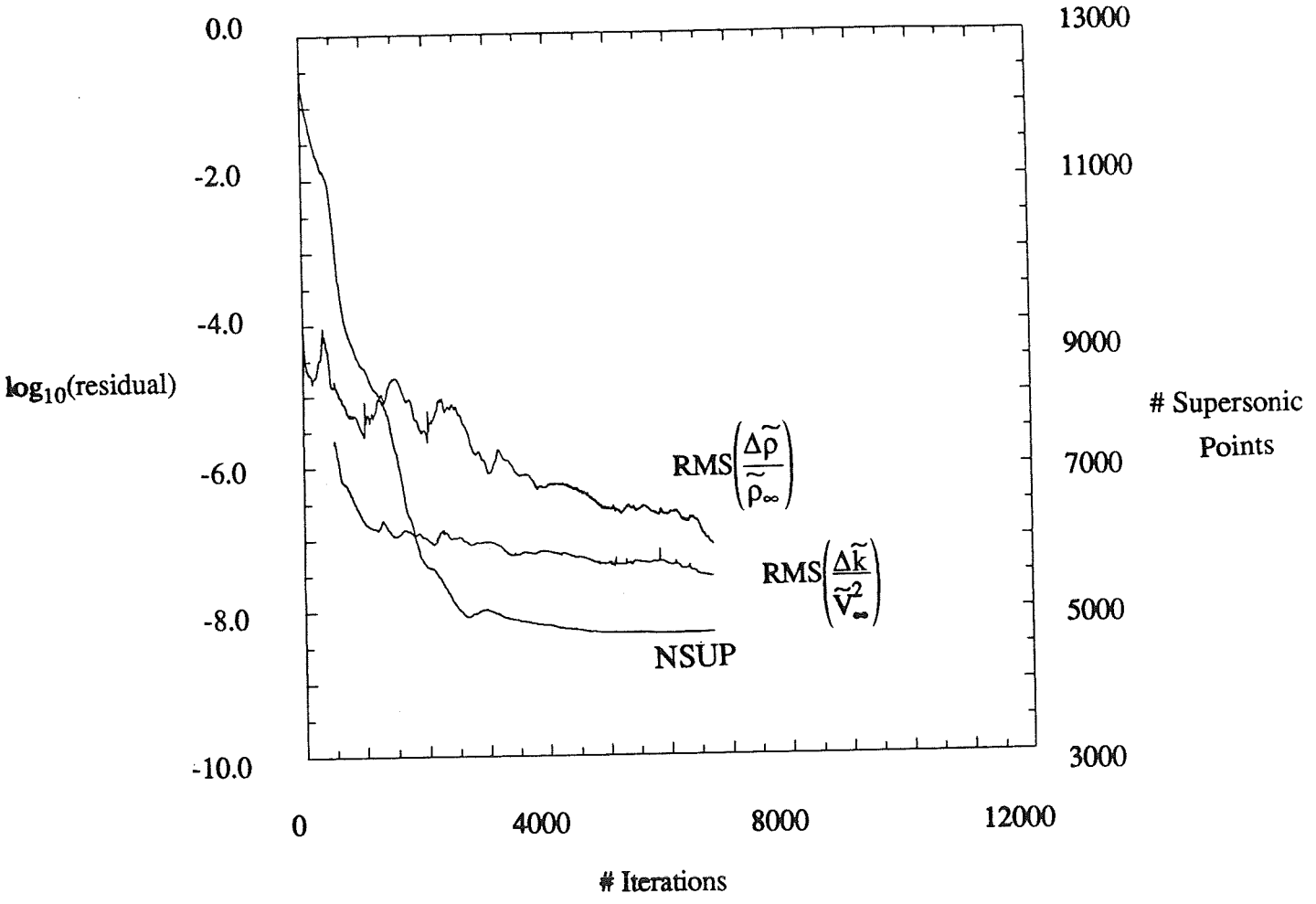

Figure 7. Convergence history for PAV-1.5 cascade computation.

In Figure 8, a hand rendering of the shock wave pattern deduced from L2F measurements has been reproduced from Reference 28, alongside the computed shock wave pattern presented as divergence of velocity contours, and Mach number contours.

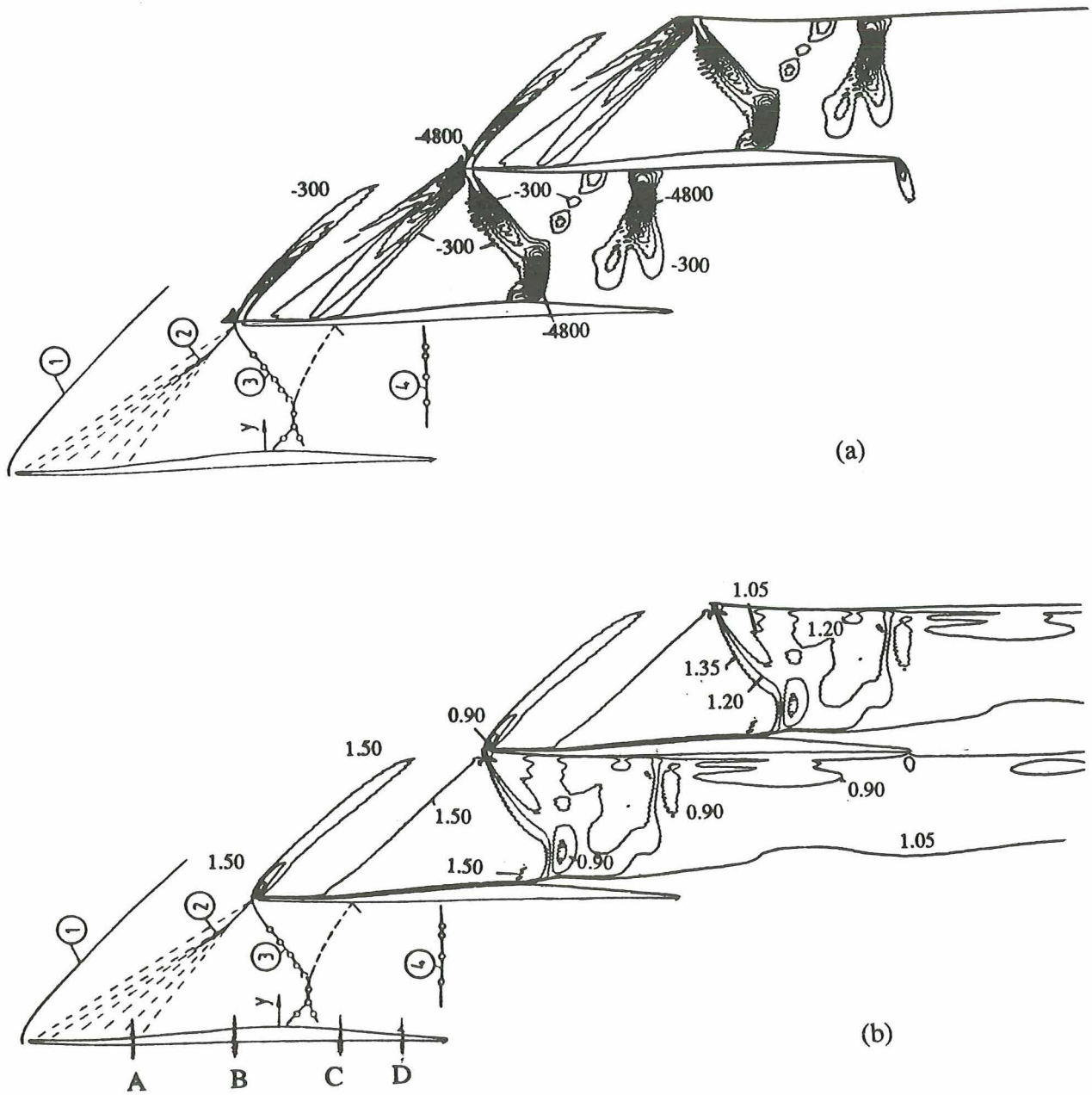

Figure 8. Shock wave pattern for PAV - 1.5 cascade. a) Divergence of velocity contours (-300 to -4800 by -500 [s^{-1}]). b) Mach number contours (0.9 to 1.5 by .15). In each diagram, the top two passages show computed contours. The bottom passage is the shock wave pattern deduced from flow visualization and L2F measurements, reproduced from Schreiber[26]. Stations labelled A-D correspond to .25, .50, .75 and .90 chord.

The key features of the flowfield are evident in this diagram, including the bow, lamda and passage shocks. In both experiment and computation, the bow shock is seen to impinge on the suction surface boundary layer of the adjacent passage. This gives rise to a lambda shock structure, a rapid thickening and separation of the boundary layer, and a Mach reflection which impinges on the pressure surface of the same passage. The high pressure ratio operating condition of this test case gives rise to a normal passage shock which impinges upstream of midchord on the pressure surface. This feature is also evident in both experiment and computation. The computation also shows some evidence of an oblique trailing edge shock, typical of supersonic compressor cascades at high operating pressure ratios.

In Figure 9, the predicted isentropic blade surface Mach number is plotted against the experimental values.

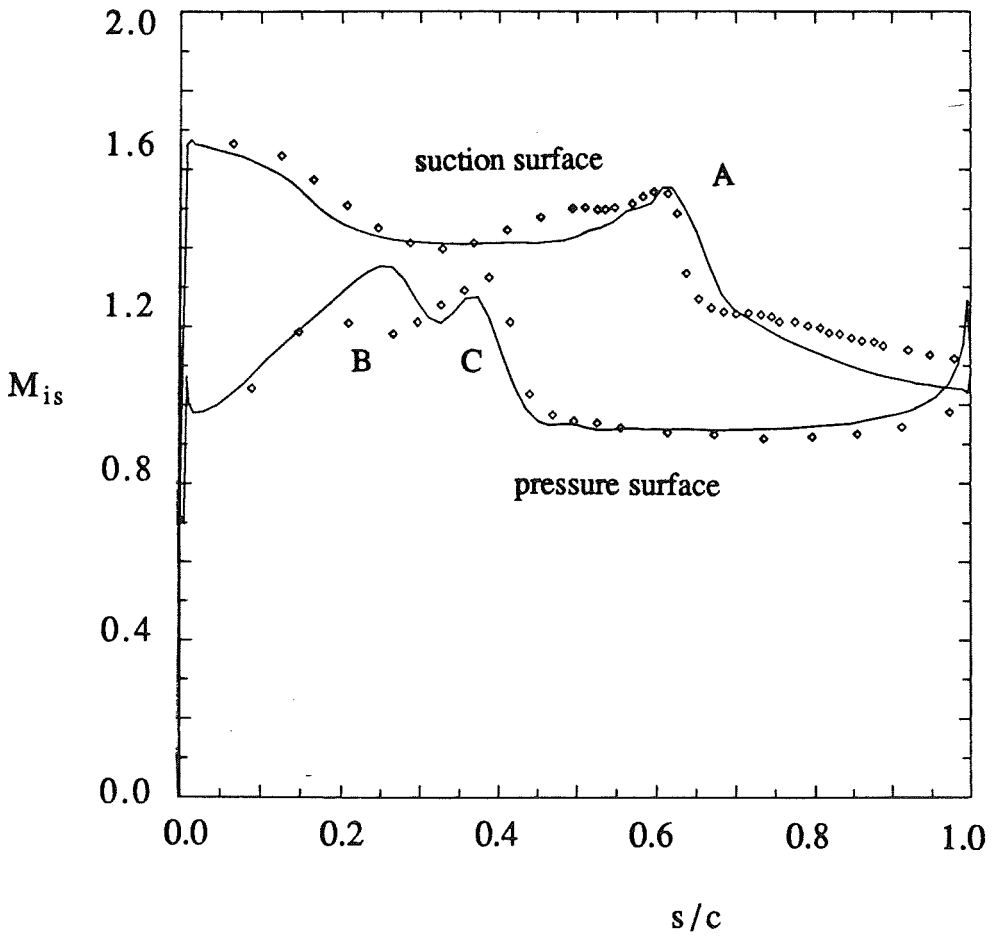

Figure 9. Isentropic blade surface Mach numbers for PAV-1.5 cascade computation. Calculated (solid line) and experimental values (symbols).

The calculation and experiment show fairly good agreement. The features labelled A, B and C in Figure 9 correspond to local compression regions where the bow shock impinges on the suction surface, the Mach reflection impinges on the pressure surface and the passage shock impinges on the pressure surface.

In Figure 10, the computed total pressure ratio is compared with traverse probe measurements at an axial location 0.09 chord downstream of the cascade exit plane.

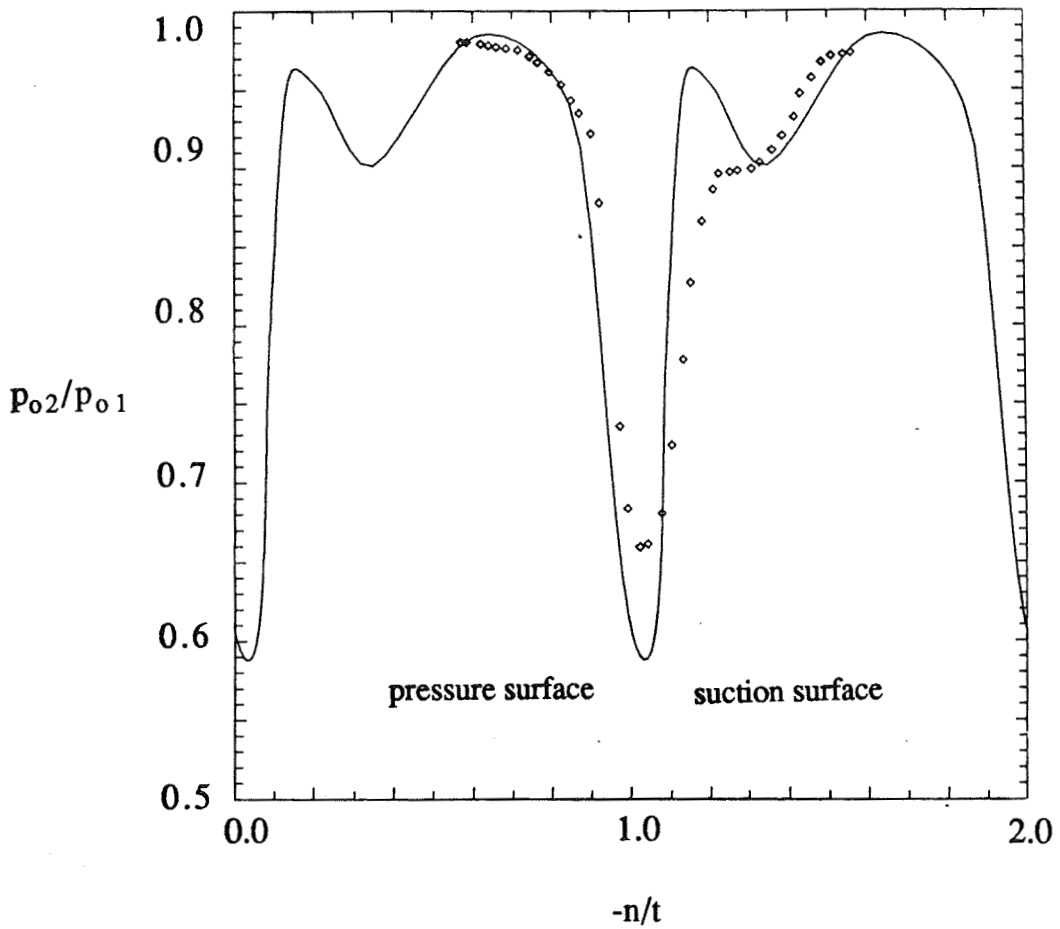

Figure 10. Total pressure ratio profile 0.09 chord downstream of trailing edge for PAV-1.5 cascade computation. Calculated (solid line) and experimental values (symbols).

The wake profile and loss distribution is reasonably well predicted, with the losses associated with the lambda shock system underpredicted. The wake centerline total pressure ratio is predicted reasonably well considering the difficulty in measurement at this location. It is noted that the results presented are not fully grid independent. Modifications in the pitchwise grid clustering near midpassage gave rise to

as much as a 2% chord difference in the impingement location of the bow shock on the suction surface and a 5% chord difference in the location of the passage shock. The loss distribution aft of the blade was hardly affected, but the blade surface Mach number distributions varied noticably.

In Figure 11, computed velocity and turbulence intensity profiles at four locations on the suction and pressure surfaces are presented.

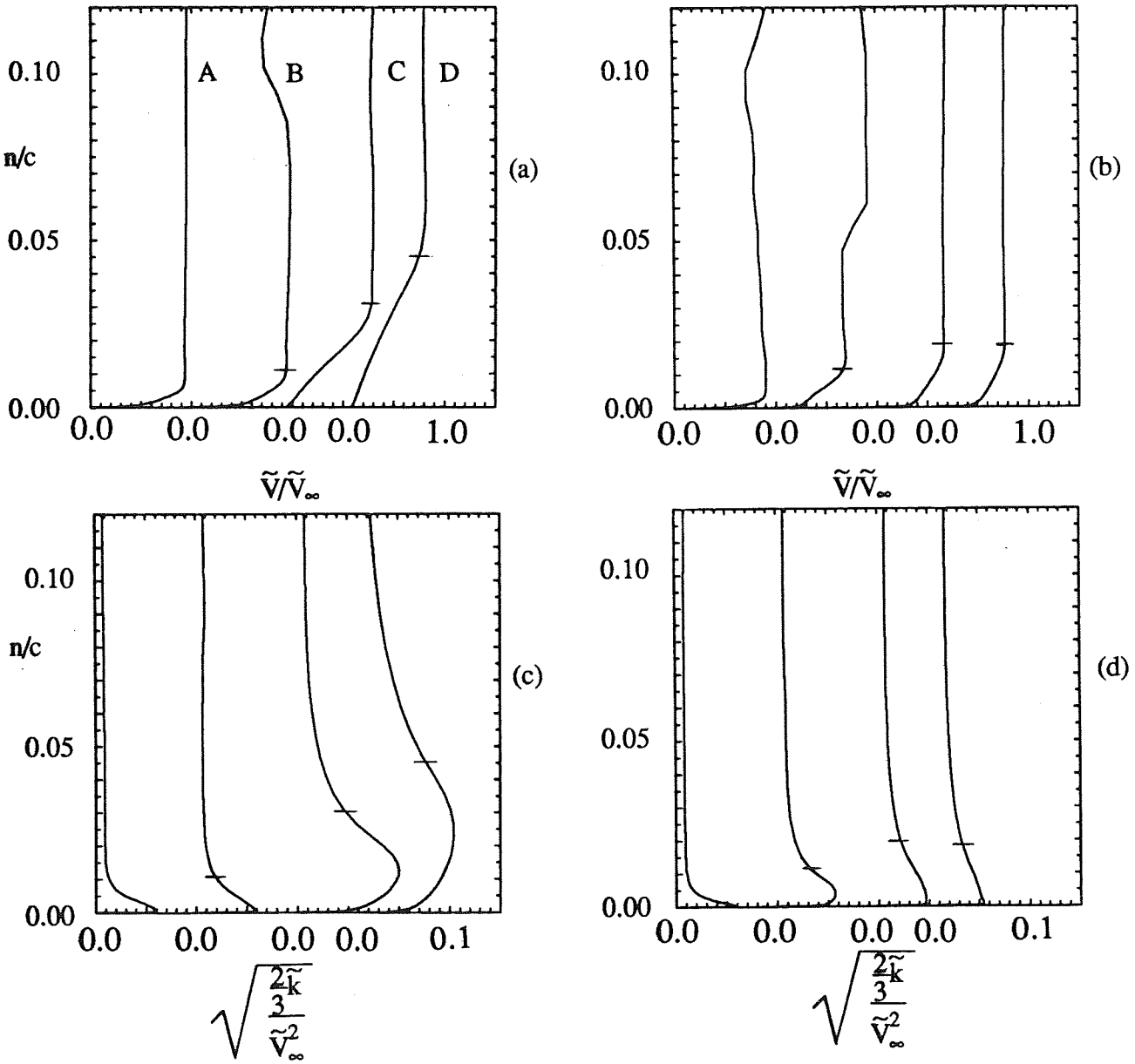

Figure 11. Local velocity and turbulence intensity profiles at four chord locations along the suction (a and c) and pressure (b and d) surfaces for the PAV-1.5 cascade computation. The hash marks correspond to the estimated boundary layer thicknesses reported by Schreiber[26]. Refer to Figure 7 for the chord locations corresponding to A-D.

Along the suction surface, the predicted boundary layer is seen to remain quite thin for this high Reynolds number flow, thickening to about .01 chord at midchord. At .75 chord the boundary layer has separated due to the bow shock impinging at .67 chord, and the boundary layer thickness is seen to have rapidly increased to approximately .03 chord. At .90 chord, the separated boundary layer has grown to .05 chord. The turbulence intensity profile behaves in a manner consistent with a boundary layer separation. Namely, aft of the onset of separation the turbulent kinetic energy boundary layer thickens rapidly and the peak in intensity appears well away from the blade surface. Careful examination of Figure 11 (c) also shows that the turbulence intensity has been amplified well outside of the boundary layer. This amplification is presumably due to the influence of the shock on the normal stress components of the production term in the turbulent kinetic energy equation.

The predicted boundary layers along the pressure surface are seen to remain quite thin along the entire blade. The influence of the passage shock at .40 chord is seen to thicken the boundary layer at .50 chord, but the flow reattaches and the boundary layer thickness remains approximately .02 chord from .75 to .90 chord. Similar trends are noticed in the local turbulence intensity profiles, with the typical peak away from the blade just aft of separation, returning very close to the wall some distance after reattachment.

The blade normal coordinate in Figure 11 is measured along grid lines which veer from perpendicular to the blade sufficiently far from the surface. The "kinks" in the velocity profiles at station B on the pressure and suction surfaces are caused by these curved grid lines intersecting the passage and bow shocks respectively.

Predicted and measured performance parameters for this cascade, operating at the given conditions are presented in Table 1.

Schreiber[26], provided measured loss coefficients at maximum attainable cascade pressure ratio for a number of operating inlet Mach numbers. For comparison, the code was run at two additional operating points within the envelope of the experimental tests. Figure 12 shows computed total pressure loss coefficients at all three operating points computed, along with the envelope of experimental loss coefficients. Computed values lie within the envelope of experimental values. It is noted, that Schreiber attributes the scatter in measured loss coefficient to variations in experimental axial velocity density ratio.

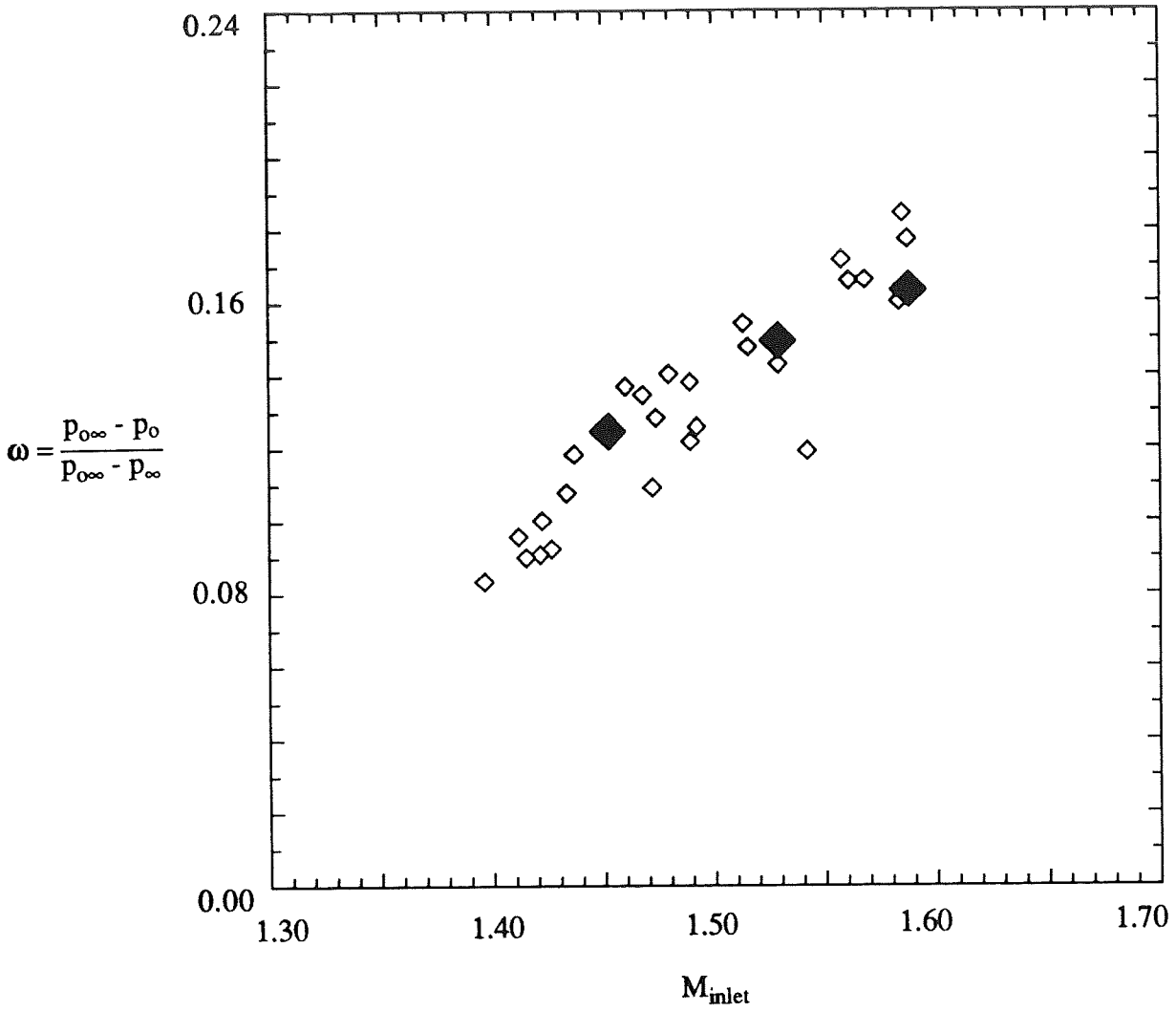

Figure 12. Total pressure loss coefficients at several cascade operating points, experiment[26] and computation (solid symbols).

ARL-Double Circular Arc Subsonic Compressor Cascade

The second cascade flow to be computed is the Applied Research Laboratory (ARL) double circular arc cascade tested at Penn State by Zierke and Deutch[29]. The computed case was tested at a negative incidence of 1.5 degrees. The working fluid was air at standard atmosphere with an inlet velocity of 32.9 m/s (inlet Mach number = 0.1). The Reynolds number based on chord was 5.0×10^5. Inlet turbulence intensity was measured at 1.8 %. The measured axial velocity ratio was measured to be between 0.97 and 1.03, indicating that the flow was close to two-dimensional.

It is noted that the present solution method, which incorporates a compressible formulation of the Navier-Stokes equations is not well suited to this low Mach number flow.

The 129 x 85 computational mesh used was generated using the GRAPE code, and is shown in Figure 13.

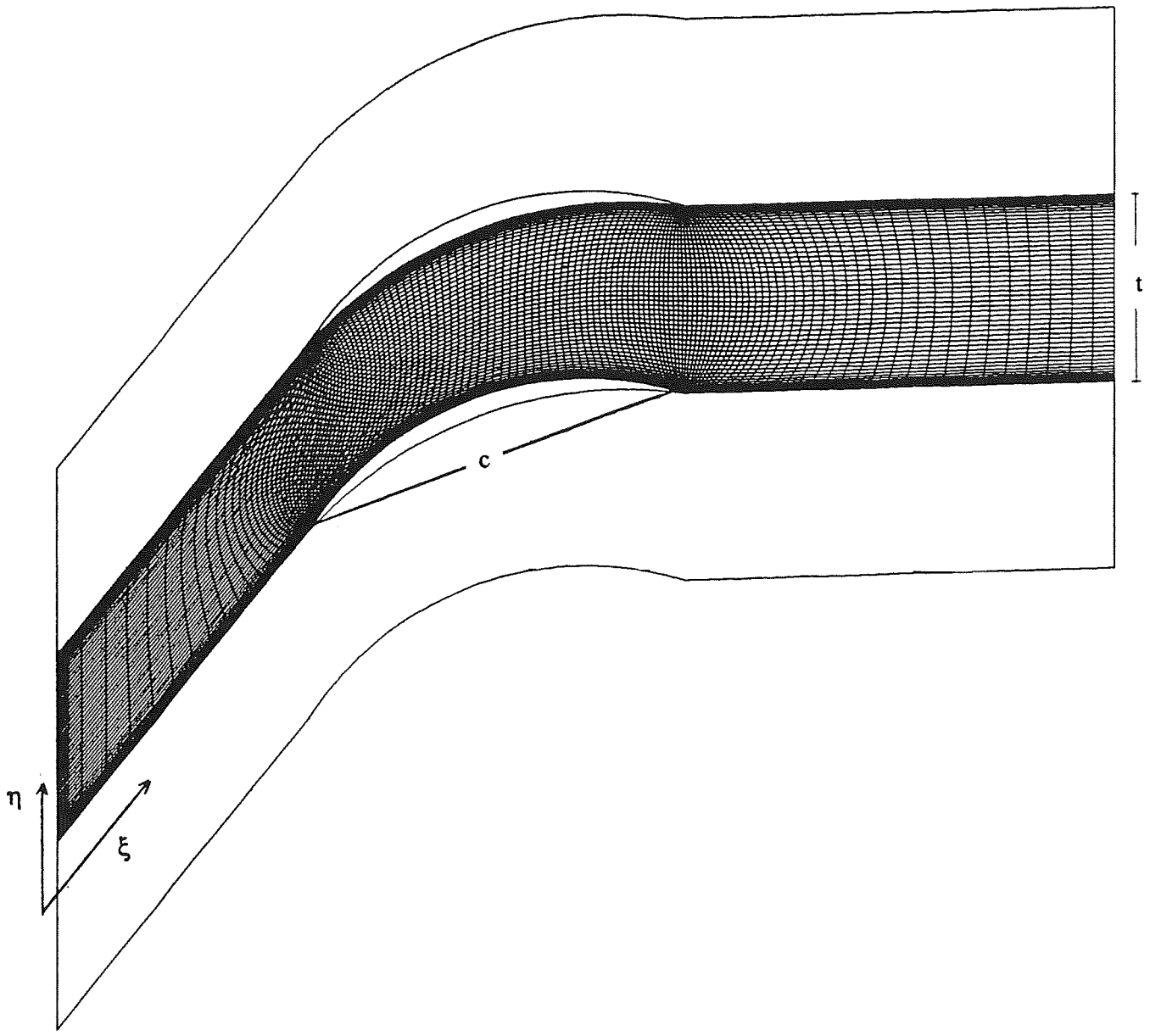

Figure 13. 129 x 85 Computational grid for the ARL DCA cascade.

Grid spacing in the blade normal direction was set to .000023 chord on the blade surfaces. This yielded values of $y^+ \leq 1$ at grid points adjacent to the walls. Except in the immediate vicinity of the leading and trailing edges, the suction and pressure surface boundary layers had at least 11 grid points with values of $y^+ \leq 20$.

It was only possible to obtain a steady solution when a coarse "preliminary" grid was used for this case. These coarse grid calculations overpredicted skin friction along the entire length of the suction surface, so the flow remain attached and a steady state solution was achieved. The more refined grid adequately resolved both inner layer and core flow regions yielding more accurate skin friction and boundary layer profiles. However, because both calculation and experiment show regions of mean flow reversal near the trailing edge, it was not possible to obtain a steady solution. The convergence history for this computation is shown in Figure 14. It took approximately 7000 iterations for this calculation to acquire a 4.5 order of magnitude drop in the RMS density residual. This corresponds to approximately 36 minutes of CPU time on the Cray Y-MP. However as shown in Figure 14, the residual changes begin to increase and then level off. This is attributed to periodic shedding of vorticity from the aft portion of the suction surface.

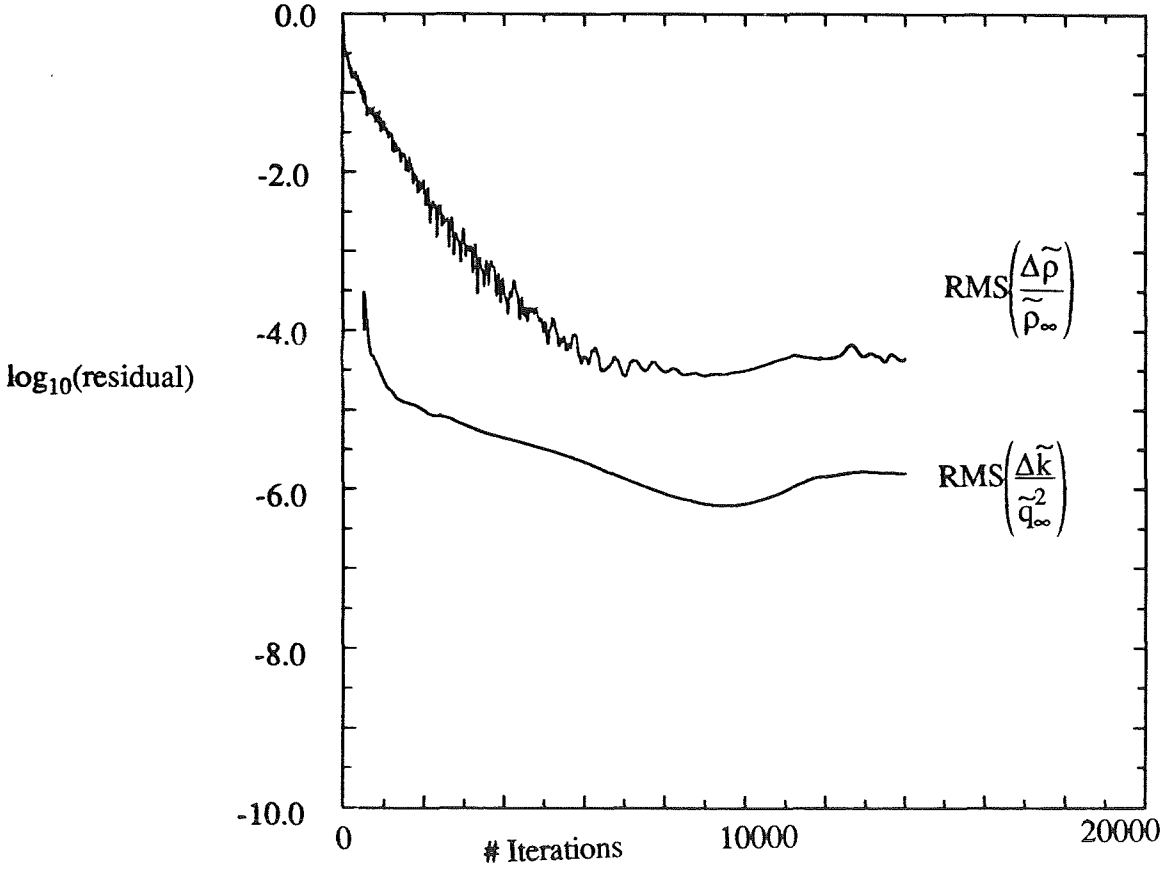

Figure 14. Convergence history for ARL DCA cascade computation.

Despite the lack of a steady state solution, the flow along the blade remained relatively unchanged after 7000 iterations except for quasi-periodic shifts in the boundary layer velocity and turbulence intensity profiles. The measured flow also showed a small region of mean backflow near the trailing edge of the blade[29], and for that reason was also probably somewhat unsteady. In Figure 15, comparison is made between computed blade surface pressure coefficient and measured values. Agreement is good along both blade surfaces.

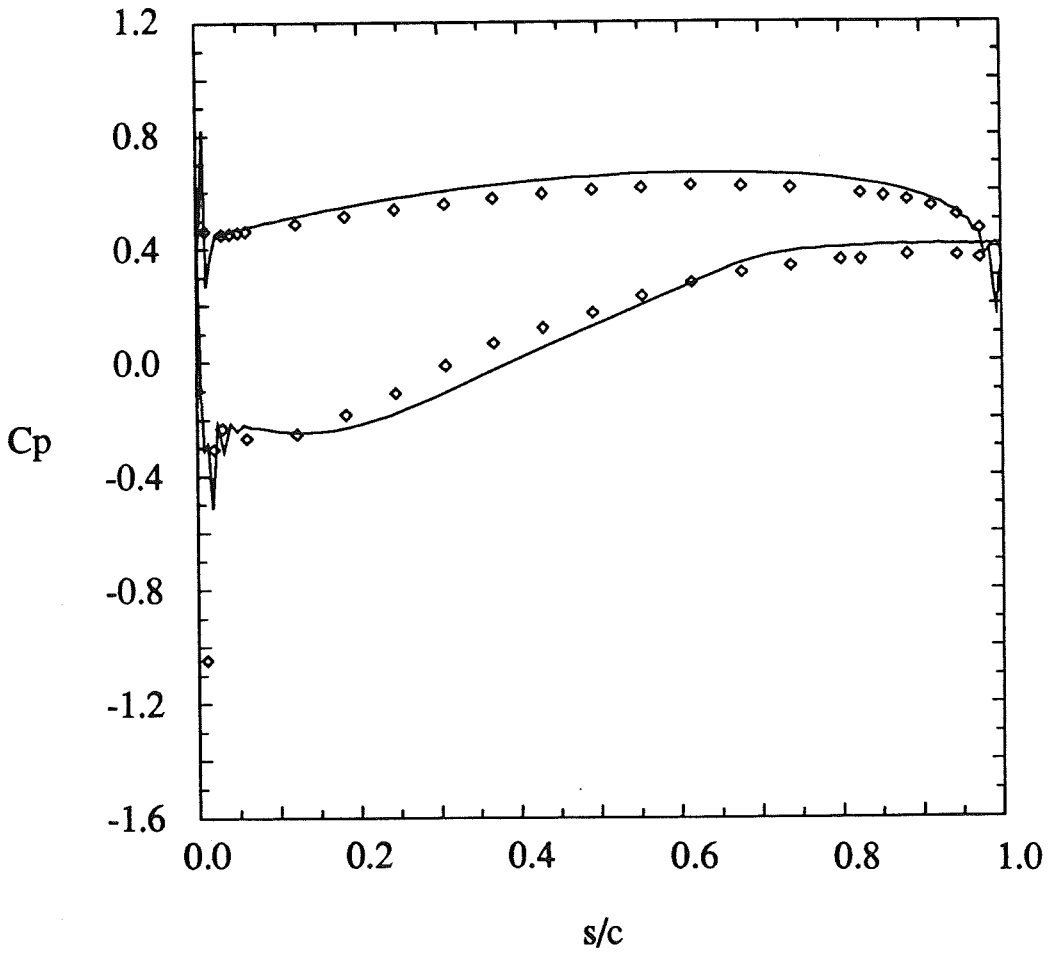

Figure 15. Pressure coefficient for ARL DCA cascade computation. Calculated (solid line) and experimental values (symbols).

The oscillations in the pressure distributions near the leading and trailing edges in Figure 15 are caused by the velocity scaling of the artificial dissipation. The H-grid used gives rise to highly skewed regions near the relatively blunt leading and trailing edges of this configuration, causing the velocity scaling presented "as is" to give rise to these oscillations. Though the cascade flow is not significantly affected by this effect, it may be worth investigating improved scaling.

In Figure 16 the predicted boundary layer profiles at three chordwise locations on the suction surface are plotted with those measured by laser doppler velocimeter. Agreement is excellent at 20 % chord and 50% chord and reasonable at 90 % chord.

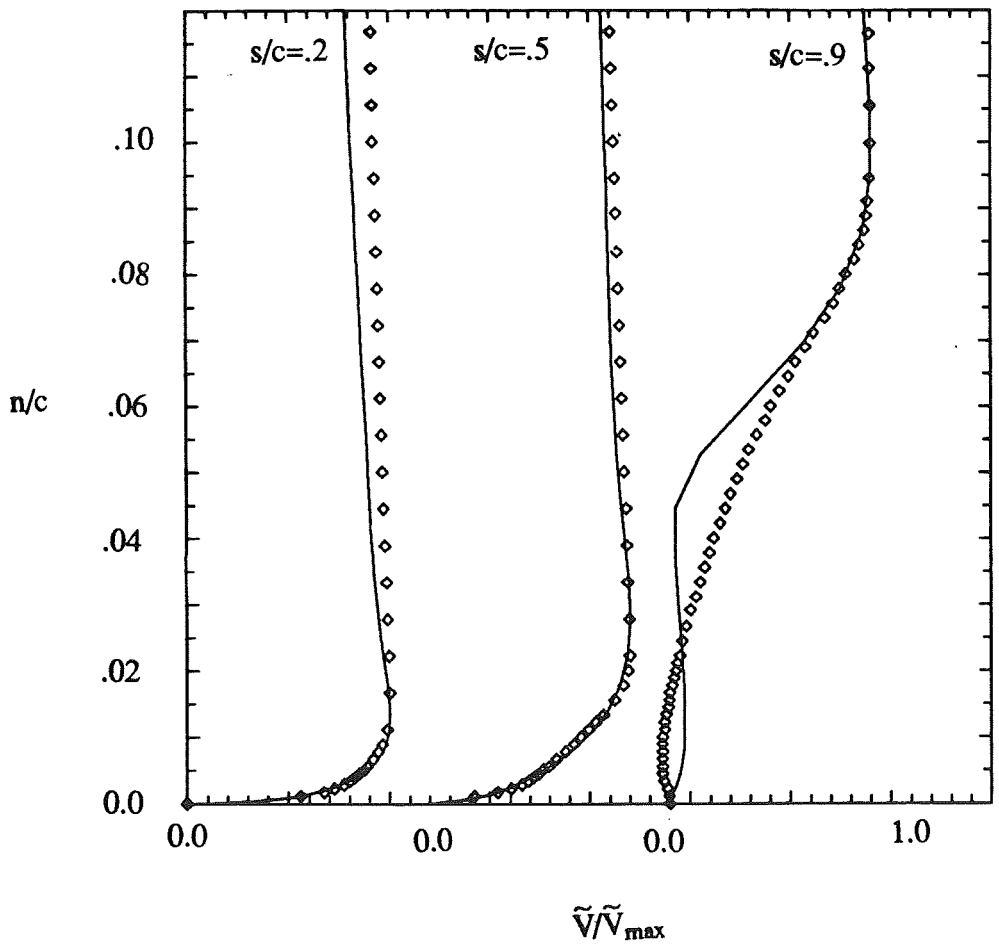

Figure 16. Boundary layer profiles at three chord locations along the suction surface for the ARL DCA cascade computation. Calculated (solid line) and experimental values (symbols).

Local turbulence intensity profiles are presented for three chordwise locations on the suction surface in Figure 17. As above, agreement between calculation and experiment is good at the first two stations, and reasonable in the aft portion of the blade.

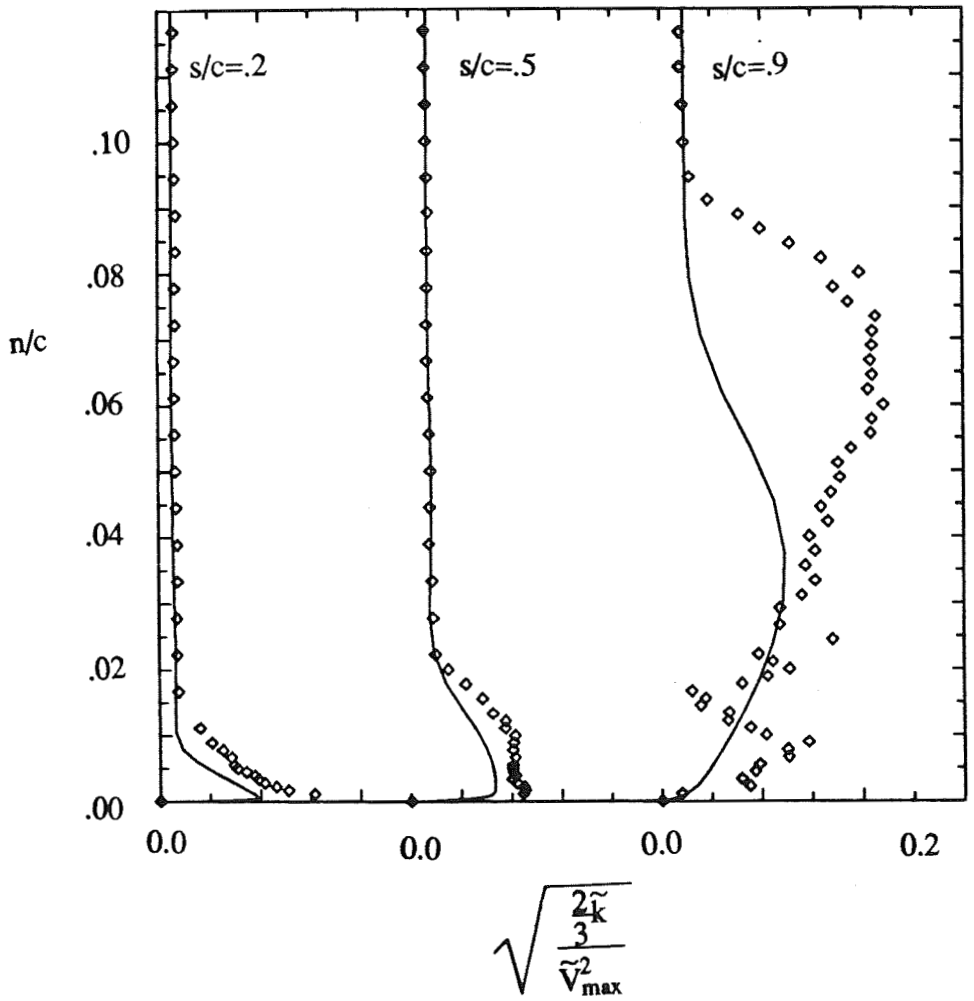

Figure 17. Local turbulence intensity profiles at three chord locations along the suction surface for the ARL DCA cascade computation. Calculated (solid line) and experimental values (symbols).

Predicted and measured performance parameters for this cascade are also presented in Table 1.

Table 1. Comparison of Cascade Flow Parameters for Computed Cases

Flowfield Parameter		PAV-1.5			ARL DCA	
	Measured	Computed	Difference	Measured	Computed	Difference
C_L [a]	$\cong$ 0.43	0.38	$\cong$ 12 %	0.82	0.88	7 %
ω [b]	0.144	.149	3.4 %	0.094	0.111	18 %
β_1	-1.8°	-1.3°	0.5°	-1.5°	prescribed	NA
β_2	2.7°	3.1°	0.4°	14.1°	13.0°	1.1°
$s/c_{sep_{ss}}$	.63	.67	6.3 %	.45	none	NA
$s/c_{sep_{ps}}$	$\cong$ 0.40	.40	$\cong$ 0.0	none	none	NA
AVDR	1.02	1	NA	0.97-1.03	1	NA

[a] lift coefficient computed from $C_L = \dfrac{(\text{Lift per unit span})_{\perp V_m}}{.5\rho_m V^2_m}$

[b] pressure loss coefficients computed from $\omega = \dfrac{p_{o\infty} - p_o}{.5\rho_\infty V^2_\infty}$ for ARL and $\omega = \dfrac{p_{o\infty} - p_o}{p_{o\infty} - p_\infty}$ for PAV.

CONCLUSIONS

A Navier-Stokes procedure has been developed and applied to a supersonic and a low subsonic compressor cascade. A compressible low Reynolds number form of the k-ε turbulence model was used. It was found in this study that :

1) A fully explicit treatment of the turbulence transport equations is possible. The computational overhead associated with this treatment is reasonable.

2) It is crucial to incorporate local timestep constraints based on stability analysis of the full viscous mean flow equations if the k-ε model is used for an H-grid cascade configuration.

3) The highly stretched grids needed to resolve near-wall physics warrant eigenvalue and local velocity scaling of artificial dissipation terms to improve accuracy and convergence rates.

4) Flowfield predictions were found to be good for a supersonic cascade and fair for a low subsonic cascade.

5) Overall cascade performance parameters were well predicted for the supersonic cascade but not well predicted for the low subsonic cascade, due to flowfield unsteadiness and turbulence model shortcomings.

Currently, several improvements and extensions to the technique are under way, including incorporation of multigridding, turbulence model corrections to account for streamline curvature and pressure strain, point implicit treatment of source terms in the turbulence transport equations, improved vectorization of the code and extension to three dimensions.

ACKNOWLEDGEMENTS

The first author was supported by a United States Army Research Office fellowship, through the grant DAAL03-86-G-0044, monitored by Dr. T. L. Doligalski. In addition, the following individuals were very helpful in providing assistance and suggestions in the course of carrying out this work : R. Chima, S. Connell, G. Dulikravich, H. Schreiber.

REFERENCES

1) Jameson, A., Schmidt, W., Turkel, E., "Numerical Solutions of the Euler equations by Finite Volume Methods Using Runge-Kutta Time-Stepping Schemes," AIAA Paper 81-1259 (1981).

2) Speziale, C. G., "Discussion of Turbulence Modelling: Past and Future," ICASE Report 89-58 (1989).

3) Lakshminarayana, B., "Turbulence Modelling for Complex Flows," AIAA Paper 85-1652 (1985).

4) Kirtley, K., Lakshminarayana, B., "Computation of Internal Incompressible Separated Flows Using a Space Marching Technique," AIAA Paper 85-1624 (1985).

5) Degrez, G., VanDromme, D., "Implicit Navier-Stokes Calculations of Transonic Shock/Turbulent Boundary-Layer Interactions," from Turbulent Shear-Layer/Shock-Wave Interactions, edited by J. Delery, IUTAM Symposium, Palaiseau, France, Springer-Verlag,1985).

6) Liu, J. S., "Navier-Stokes Cascade Analysis With the k-ε Turbulence Model," Ph.D. Thesis, MAE, Case Western Reserve University (1987).

7) Grasso, F., Speziale, C. G., "Supersonic Flow Computations by Two-Equation Turbulence Modelling," AIAA Paper 89-1951 (1989).

8) Eliasson, P., "Solutions to the Navier-Stokes Equations Using a k-ε Turbulence Model," Flygtekniska Forsoksanstalten TN 1988-19, Stockholm (1988).

9) Holmes, D. G., Connell, S. D., "Solution of the 2D Navier-Stokes Equations on Unstructured Adaptive Grids," AIAA Paper 89-1932 (1989).

10) Favre, A., "Equations des Gaz Turbulents Compressibles: 1. Formes Generales," Journal de Mechanique, Vol. 4 (1965).

11) Jones, W. P., "Models for Turbulent Flows with Variable Density and Combustion," from Prediction Methods for Turbulent Flows, edited by W. Kollmann, Hemisphere (1980).

12) Chien, K., "Predictions of Channel and Boundary-Layer Flows with a Low-Reynolds-Number Turbulence Model," AIAA Journal, Vol. 20, No.1, January (1982).

13) Coakley, T. J., "Turbulence Modelling Methods for the Compressible Navier-Stokes Equations," AIAA Paper 83-1693 (1983).

14) Nichols, R. H., "A Two-Equation Model for Compressible Flows," AIAA Paper 90-0494 (1990).

15) Hobson, G. V., Private Communication (1989).

16) Jones, W. P., Launder, B. E., "The Prediction of Laminarization With a Two-Equation Model of Turbulence," International Journal of Heat and Mass Transfer, Vol. 15 (1972).

17) Martinelli, L., "Calculation of Viscous Flows with Multigrid Methods," Ph.D. Thesis, MAE Department, Princeton University (1987).

18) Pulliam, T. H., "Artificial Dissipation Models for the Euler Equations," AIAA Journal, Vol. 24, No. 12, December (1986).

19) Caughey, D. A., Turkel, E., "Effects of Numerical Dissipation on Finite Volume Solutions of Compressible Flow Problems," AIAA Paper 88-0621 (1988).

20) Swanson, R., Turkel, E., "Artificial Dissipation and Central Difference Schemes for the Euler and Navier-Stokes Equations," NASA CR-178296 (1987).

21) Radespiel, R., Swanson, R., "An Investigation of Cell Centered and Cell Vertex Schemes for the Navier Stokes Equations," AIAA Paper 89-0548 (1989).

22) Davis, R. L., Ni, R., Carter, J. E., "Cascade Viscous Flow Analysis Using the Navier-Stokes Equations," AIAA Paper 86-0033 (1986).

23) Swanson, R., Private Communication (1990).

24) Chima, R. V., Johnson, G. M., "Efficient Solutions of the Euler and Navier-Stokes Equations With a Vectorized Multiple-Grid Algorithm," AIAA Journal, Vol. 23, No. 1, January (1985).

25) Baldwin, B. S., Lomax, H., "Thin Layer Approximation and Algebraic Model for Separated Turbulent Flows," AIAA Paper 78-257 (1978).

26) Schreiber, H. A., "Experimental Investigations on Shock Losses of Transonic and Supersonic Compressor Cascades," AGARD CP-401, Paper No. 11 (1988).

27) Sorenson, R. L., "A Computer Program to Generate Two-Dimensional Grids About Airfoils and Other Shapes by the Use of Poisson's Equation," NASA TM-81198 (1980).

28) Gorski, J., "Generation of H-Type Grids Using the GRAPE Code," Internal Memo, Department of Aerospace Engineering, Penn State University (1983).

29) Zierke, W. C., Deutsch, S., "The Measurement of Boundary Layers on a Compressor Blade in Cascade: Part 4 -- Flow Fields for Incidence Angles of -1.5 and -8.5 Degrees," ASME Paper 89-GT-72 (1989).